Femtosecond wave packet spectroscopy: Coherences, the potential, and structural determination

M. Gruebele[a)] and A. H. Zewail
Arthur Amos Noyes Laboratory of Chemical Physics, California Institute of Technology, Pasadena, California 91125

Recently, we presented a formalism for extracting highly resolved spectral information and the potential of bound isolated systems from coherent ultrafast laser experiments, using I_2 as a model system [Gruebele *et al.*, Chem. Phys. Lett. **166**, 459 (1990)]. The key to this approach is the formation of coherent wave packets on the potential energy curve (or surface) of interest, and the measurement of their *scalar* and *vector* properties. Here we give a full account of the method by analyzing the coherences of the wave packet in the temporal transients of molecules excited by ultrashort laser pulses, either at room temperature, or in a molecular beam. From this, some general considerations for properly treating temporal data can be derived. We also present a direct inversion to the potential and quantum and classical calculations for comparison with the experiments.

I. INTRODUCTION

The creation of coherent wave packets by an ultrashort laser pulse is essential for time-resolved studies of the nuclear motion in chemical reactions.[1] For nonreactive isolated systems, these packets are in bound (or quasibound) potentials, where they may undergo periodic oscillations, dephasing, and recurrence. A question of interest, particularly for structural determination, is the following: How can such an ultrashort pulse "see" the vibrational/rotational eigenstates of a bound potential? The key is that the pulse has sufficient bandwidth to form a *coherent* superposition of eigenstates with a well-defined phase evolution. The resulting wave packet shows some spatial localization, and if its motion can be observed temporally, all the spectroscopic information (e.g., vibrational and rotational level structure) can be obtained. With picosecond pulses, coherence has been probed in isolated molecules to study rotational dynamics (structural determination) and intramolecular vibrational energy redistribution (IVR).[2] With femtosecond pulses, a much broader range of vibrational and rotational dynamics becomes accessible, due to the formation of larger bandwidth wave packets.[3]

The time resolution is now sufficient to separate the nuclear vibrational and rotational motions. Just as NMR, ESR, microwave, and visible spectroscopy have benefited from pulsed techniques (in the form of FT-NMR, FT-ESR, FT-microwave, and quantum beat[4] spectroscopies) with bandwidths in the kHz to GHz region, it is now possible to open a spectral window in the THz region with lasers ranging from the ir to the near uv and beyond.

Previously, we addressed the question of how highly resolved spectroscopic information can be obtained from fs pulse excitation despite their broad spectral bandwidth, by studying the coherences observed in the transient.[5,6] In the following, we will consider the model system I_2 (in the B electronic state) and compare theory with experiments. The high-resolution spectroscopy of I_2 is well known,[7] and rovibrational wave packets can easily be created;[8] this molecule is therefore an ideal benchmark for the type of information that can be extracted by time-resolved techniques. We show that vibrational and rotational coherences can be separated experimentally. The wave packet dynamics yield direct information about the vibrational and rotational motion (as well as rovibrational couplings), allowing one to obtain the potential. With a small number of such femtosecond measurements (less than ten in the present case) spanning a wide range of the spectrum (from the term energy to the dissociation limit of the B state in the present case), we are able to obtain excellent agreement with results in the literature. As with rotational coherence spectroscopy, the wave packet approach promises to be powerful for bound potentials, especially in larger molecular systems.

The results illustrate two points. First, the spectroscopy and potentials of bound systems can be obtained from wave packet dynamics with a separation of time scales for the vibrational and rotational motions. This separation, which can also be made by measurements of the scalar and vector properties of the dynamics, simplifies the analysis considerably. Also, coherences are formed only on the potential of interest and there are no complications from the other states involved in the transitions. Second, the correspondence made here between high resolution spectra and time-resolved spectra is valid if one is considering simple systems. For chemical reactions with *intermediates* or large complex systems, this correspondence is not as valid in practice.

We will first outline the experimental approach, and then provide a general description of the wave packet motion for the case at hand. To apply them to real systems, several simplifications can first be made which greatly enhance the usefulness of the formalism and the physical picture to be gleaned from it. With these considerations, we are then equipped to consider applications to real systems.

[a)]Present address: School of Chemical Sciences, University of Illinois at Urbana-Champaign, 505 So. Mathews Ave., Urbana, IL 61801.
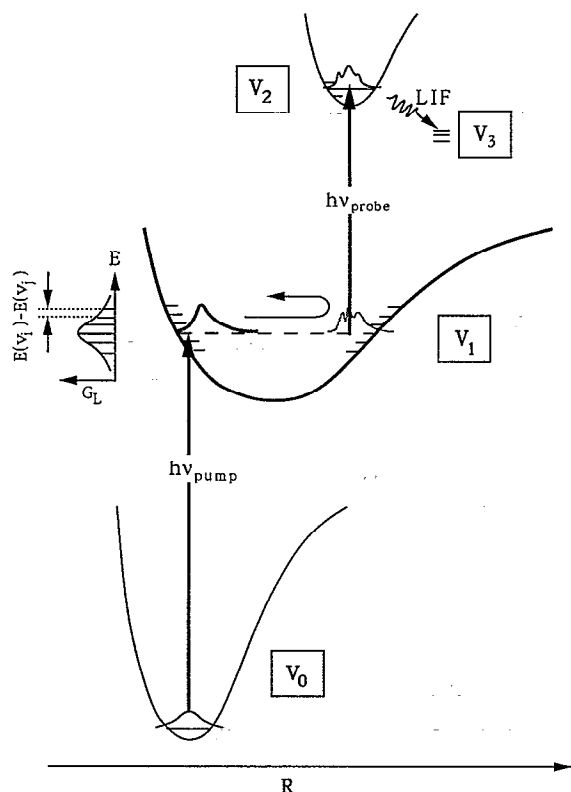
FIG. 1. Schematic of the femtosecond pump–probe experiment for a bound potential; the wave packet formed on the intermediate surface (V_1) consists of a number of eigenstates covered by the laser bandwidth G_L, and with characteristic frequencies $E(v_i) - E(v_j)$; these frequencies are preserved in the coherence of the transient obtained by probing the packet to a final surface (V_2), from where it can be detected by LIF to V_3 (or through mass spectrometry or other means).

We conclude with time-dependent quantum calculations, to show how molecular rotation and vibration under beam or gas-cell conditions affect the observed coherence.

II. THE FEMTOSECOND WAVE PACKET APPROACH

The methodology of the experiments has been described in detail elsewhere.[8] Here we discuss the physical picture of the laser–molecule interactions, and the appearance of the time-resolved transients obtained.

Figure 1 shows the potential energy function for I_2, for a typical pump-probe experiment with an initial pulse at 550 nm and a second pulse at 310 nm. The experiment starts from an incoherent superposition of initial states, described in the simplest case by a single temperature, and requiring in general a number of "effective" translational/rotational/vibrational temperatures or a more general density matrix description. This incoherent superposition is pumped by an ultrashort pulse of bandwidth $\Delta\omega$ (coherence width of a transform-limited pulse) into a coherent superposition, resulting in a wave packet (or more properly, a partially coherent "density-matrix packet") moving on the excited state surface (the B state, in I_2). If the laser bandwidth $\Delta\omega$ is properly matched to the energy-level sep-

aration of the molecular Hamiltonian, a close to "minimum uncertainty" wave packet can be produced, which moves very much like an ensemble of classical particles at short times.

Whether the wave packet can be approximated semiclassically, or whether it is thoroughly quantal in nature, its motion, which is a reflection of its coherence properties, can be imaged by a second laser pulse onto a higher electronic state (here the ion-pair f state of I_2).[9] From a spectral perspective, the phases of the Franck–Condon factors (FC, including in this discussion a time-dependent phase) for the probe transition can interfere constructively or destructively, depending on the location of the wave packet on the intermediate surface. Of course, this does not imply that pumping with ultrashort pulses can create a strong transition in a wavelength region where none existed in a cw experiment, simply by shifting the wave packet to a better position, but the FC factors can interfere to yield transitions several times stronger or weaker (depending on the number of levels involved in the coherence) than the cw average, and oscillating about that average as a function of pump–probe delay. Note also in Fig. 1 that the pump as well as probe transitions tend to conserve the kinetic energy of the wave packet, at least in the semiclassical limit under resonant-transition conditions (extended FC principle for wave packets).

The coherence in the intermediate state is thus probed as a function of the time delay between pump and probe pulses. In practice, this is accomplished by scanning one of the pulses on a calibrated translation stage. As seen in Sec. IV, this calibration, rather than the temporal length of the coherent transient, can be the factor limiting accuracy. The type of transient obtained in the specific case of I_2 is shown in Fig. 2(a). The vibrational motion of the wave packet yields rapid oscillations at early times, which are damped because the vibrational frequencies are not commensurate, and because the rotation–vibration coupling shifts the vibrational frequencies as the rotational excitation increases. At long times, the rotating dipoles realign (if polarized laser excitation was used), with a period determined by the rotational constants in the various vibrational levels populated by the pump pulse pure rotational coherence.[10]

After the probe pulse, the population in the final state can be detected as cw fluorescence,[11] a multiphoton ionization (MPI) signal,[12] or by chemical reaction means.[13] The partial coherence thus loses nearly all information about the initial or final electronic states, since only the coherence in the intermediate state is probed at different times by the second laser pulse. This can be an advantage, since it allows one to do spectroscopy on a *single* potential function (or surface, PES, in general) at a time. Furthermore, as discussed in Sec. IV, it makes the determination of molecular parameters *independent* of the laser wavelengths and profiles, which is desirable, since these quantities need then not be accurately determined. The coherence preserves all the relative spectral information (e.g., vibrational frequency differences) of the intermediate state, which is sufficient to characterize that state (except for its term energy).
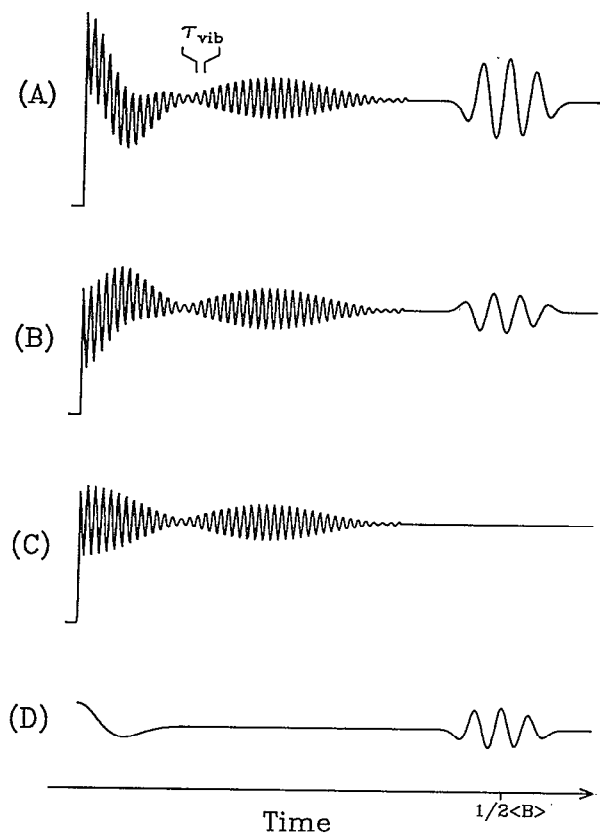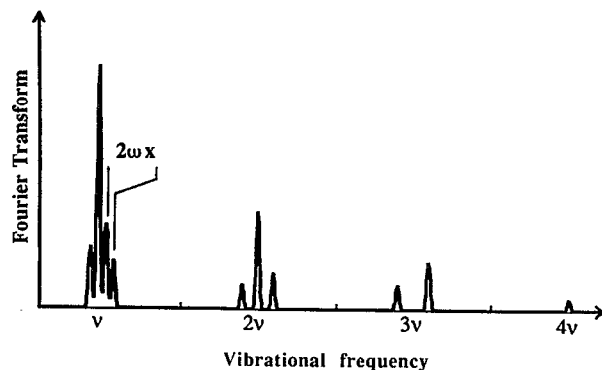
FIG. 3. Amplitude spectrum of the vibrational transient in Fig. 2(c); in I_2, there is a cluster at the local vibrational frequency, corresponding closely to the several vibrational band origins covered by the laser profile; at higher frequencies, the cluster is repeated with successively fewer lines, corresponding to energy differences between levels separated by Δv $=2,3\cdots$.

FIG. 2. Separation of rotations and vibrations by time scale and polarized detection; (A) shows a transient obtained in parallel detection, (B) one in perpendicular detection; (C) corresponds to magic angle detection, which removes both early time and later time rotational anisotropies; (D) corresponds to anisotropic detection (parallel minus perpendicular), showing only the rotational effects; as discussed in the text, rotation–vibration couplings still affect the envelope of transient (C) even in magic-angle detection.

Thus if one were to determine the power spectrum of the vibrational transient 2(c), it might appear as shown in Fig. 3; a cluster of lines near the fundamental vibrational spacing ω, another weaker cluster at 2ω (weaker due to the chosen finite spectral bandwidth of the laser and rotation-vibration couplings), a weaker one still at 3ω, and so forth. It is clear that these peaks should correspond to vibrational frequencies in the intermediate electronic state, but it remains to be seen in Secs. III C and IV how precise vibrational constants can be extracted from the transient in Fig. 2(c).

The incoherent effects of the initial ensemble can be almost eliminated by using a molecular beam, where a minimal number of rotational and vibrational levels of the ground state are populated.[12] Such cooling is usually advantageous in high resolution spectroscopy, where collimated molecular beams are used to reduce spectral congestion and Doppler broadening. As will be seen below when comparing cell and molecular beam results, femtosecond wave packet spectroscopy (FWS) actually works best at higher temperatures, where it extracts the most information, especially for small systems. By its nature as a coherent rather than a spectral experiment on a time scale

smaller than any molecular collisions, it removes the problem of Doppler broadening. For example, rotational constants can be read off directly from the recurrence time, and determined to some fractional accuracy, even when they are very small (below the resolution of a cw experiment); also, the molecular frequencies contained in a rovibrational coherence are unchanged, since the Doppler effect only shifts the laser frequency and bandwidth in the molecular frame, causing a slightly different set of energy levels to be overlapped.

A further consequence of this spectroscopy is a separation of time scales, and a convenient separation of scalar and vector effects in the molecular motion, as mentioned above. Vibrations generally occur on a femtosecond time scale, while rotations occur on a time scale of 10 to 1000 ps, depending on the force constants, geometries, and masses involved. Spin–orbit splittings and other effects may occur on even longer time scales, from 1 to 1000 ns. As shown in Fig. 2(a), the rotational and vibrational time scales in I_2 are indeed very different. Furthermore, polarized detection can eliminate either scalar (e.g., vibrational) or vector (e.g., rotational) effects [Figs. 2(b)–2(d)], depending on the angle between the two laser pulse electric fields (and the detector).[1]

As discussed below, this does not, of course, eliminate the rotation–vibration interactions inherent in the molecular Hamiltonian, which must still be considered in a detailed analysis. The most obvious manifestation in Fig. 2(a) is the fact that, while the rotational constant can be seen to be approximately $1/2t_R$ (t_R being the time for a full rotational recurrence), there are several peaks corresponding to the several vibrational states present in the superposition (and also the centrifugal distortion interaction, as discussed in Ref 5). However, it will be seen below that the vibrational (early time) and rotational (long time) transients can always be treated separately from one another, in effect decoupling the simultaneously obtained rotational and vibrational information.
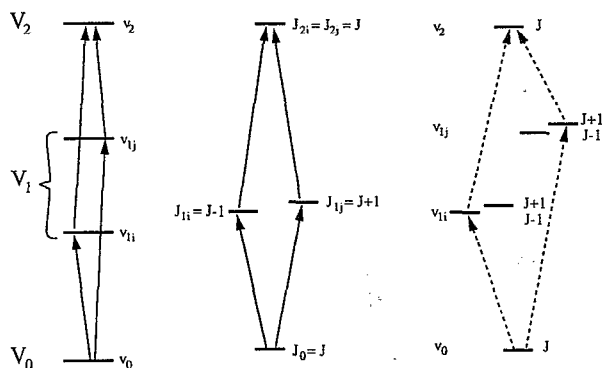
FIG. 4. Schematic representation of two-level quantum interference; (left) vibrational; (middle) rotational; (right) 2 by 2 level rotation–vibrational; V_0, V_1, and V_2 refer to the electronic potential surfaces on which the levels lie, v_0, v_1, v_2 are the corresponding vibrational quantum numbers.

III. COHERENCES: VIBRATIONAL AND ROTATIONAL

The general formalism of quantum coherence relevant to the present work has been discussed in a number of articles (see, e.g., Refs. 10, 14, and 15). Here, we consider first a simple picture, and then a more general formulation. A number of simplifications are made, which will elucidate the underlying physics and provide a more effective framework for analyzing actual experimental data by highlighting the important features.

A. Simple picture

Consider Fig. 4(a), for the case of a vibrational two-level system ($|v_{1i}\rangle$ and $|v_{1j}\rangle$ on surface V_1) accessed by a pump pulse from a single vibrational level $|v_0\rangle$. After the pulse, the part of the state of interest evolves as

$$|\Psi_1\rangle \sim a_{01}(v_{1i})e^{-i2\pi c E_1(v_{1i})\tau}|v_{1i}\rangle$$
$$+ a_{01}(v_{1j})e^{-i2\pi c E_1(v_{1j})\tau}|v_{1j}\rangle, \quad (1)$$

where energies and frequencies are in cm^{-1}. We are excluding here coherences between the V_0 and V_1 surfaces, which are possible in principle, but not probed in the present experiments. (With a stable-enough interferometer, this may be possible.) The factors a_{01} depend on the laser electric field and transition dipole moment, $a_{01} \propto G_{L01}\mu_{01}$.

In order for a coherence to be observed, the probe pulse must excite both components of the wave function to the same state $|v_2\rangle$, which may be detected by LIF, for example. Again neglecting coherences between V_2 and V_1, we obtain for the final signal

$$I(t) \sim |\langle v_2|G_{L12}\mu_{12}|\Psi_1\rangle|^2$$
$$\propto a_{01}(v_{1i})^2 a_{12}(v_{1i})^2 + a_{01}(v_{1j})^2 a_{12}(v_{1j})^2$$
$$+ 2a_{01}(v_{1i})a_{12}(v_{1i})a_{01}(v_{1j})a_{12}(v_{1j})$$
$$\times \cos(2\pi c[E_1(v_{1j})-E_1(v_{1i})]\tau)$$
$$= c_i^2 + c_j^2 + 2c_i c_j \cos(2\pi c[E_1(v_{1j})-E_1(v_{1i})]\tau), \quad (2)$$

which contains oscillations due to coherence in V_1. Coherence effects due to V_0 and V_2 are eliminated since phase incoherent pulses and time-independent detection of the final state are used, yielding a spectroscopy with frequency components sensitive to only the intermediate surface. The above results are reminiscent of those obtained in the studies of IVR[2] and highlight the nature of the phase shift, depending on the detection scheme, and the modulation depth, depending on the c's.

Collecting the c's in a constant A_{Vij}, it is easily seen that for more levels, one obtains for the oscillatory part

$$I_V(t) \sim 2\sum_{ij} A_{Vij}\cos(2\pi c[E_1(v_{1i})-E_1(v_{1j})]\tau). \quad (3)$$

A similar response is found for two rotational levels,[2,10] as shown in Fig. 4(b). Here the application of the vector dipole model yields J-dependent amplitude factors. For example, for parallel transitions (diatomic or linear molecule) with selection rules $\Delta J = \pm 1$ and two laser pulses with parallel relative polarizations, the cross term analogous to Eq. (2) becomes

$$I_R(t) \sim \frac{2}{15}\frac{J(J+1)}{2J+1}\cos(2\pi c[E(J+1)-E(J-1)]\tau),$$
$$(4)$$

including the M-level degeneracy of the $|J_0=J\rangle$ initial state. The generalization to a sum over a large number of J levels, usually weighted by a Boltzmann factor, is again clear.

In the most general case, cross terms between rotation and vibration must be considered, as in the 2×2 rovibrational level system in Fig. 4(c). For each vibrational coherence v_1/v_1+1, there are now four rotational terms contributing, namely, $J+1/J+1$, $J-1/J-1$, $J+1/J-1$, and $J-1/J+1$ [the last shown in Fig. 4(c)]. The first two contain no rotational anisotropy (but do contain vibration–rotation interaction, since they are still J dependent), and do not cancel in magic-angle detection; the latter two result in rotational anisotropy, and cancel in magic angle detection.

B. General picture

For generalization we shall use the density matrix approach, invoked before in the description of rotational and vibrational coherence on the picosecond time scale.[2,10,14,15] For femtosecond pump–probe methodology, Mukamel has shown the power of the method in describing observables and Lin and Mathies have developed applications to temporal and spectral studies.[16]

Since the final detection step, whether optical, mass analyzed, or chemical, does not preserve any coherence of the *final* (third) electronic state of the pump–probe sequence, the detected signal is proportional to a weighted sum of the populations in each of the final eigenstates. Consider LIF detection as an example (Fig. 1). Emission takes place to a fourth state (or set of states), and the weighting factor $O(q_2)$ (with appropriate units) for a single state in V_2 is a convolution of all its transition strengths

for emission with a wavelength-dependent response function of the detection system. This corresponds to a weighted trace over the density matrix describing the final state,

$$I(\tau) = \mathrm{Tr}_{\{q_2\}}[O(q_2)\rho(\tau)], \tag{5}$$

where $\{q_2\}$ indicates a trace over all quantum numbers describing the system after the probe pulse (e.g., v_2, J_2, and M_2 quantum numbers in the f state of I_2), and τ is the time lag between the pump and probe pulses which yields the time-dependent coherent transient $I(\tau)$.

One obtains for $\rho(\tau)$, using the standard density matrix formalism, the symmetrical expression

$$\rho(\tau) \sim \sum_{\substack{v_{2i}J_{2i}M_{2i} \\ v_{2j}J_{2j}M_{2j}}} \sum_{v_{1i}J_{1i}M_{1i} \atop v_{1j}J_{1j}M_{1j}} \sum_{v_0 J_0 M_0} |J_{2i}M_{2i}\rangle\,|J_{2i}v_{2i}\rangle e^{-i2\pi c E_2(v_{2i},J_{2i})t+\phi_{12}} \times G_{L12}[E_2(v_{2i},J_{2i})-E_1(v_{1i},J_{1i})-\omega_{12}]$$

$$\times \langle J_{2i}M_{2i}|\hat{z}\cdot\begin{Bmatrix}\hat{Z}\\\hat{X}\end{Bmatrix}|J_{1i}M_{1i}\rangle\langle J_{2i}v_{2i}|\mu_{12}(r)|J_{1i}v_{1i}\rangle\omega_{12} e^{-i2\pi c E_1(v_{1i},J_{1i})\tau+\phi_{01}}$$

$$\times G_{L01}[E_1(v_{1i},J_{1i})-E_0(v_0,J_0)-\omega_{01}]\langle J_{1i}M_{1i}|\hat{z}\cdot\begin{Bmatrix}\hat{Z}\\\hat{X}\end{Bmatrix}|J_0 M_0\rangle\langle J_{1i}v_{1i}|\mu_{01}(r)|J_0 v_0\rangle\omega_{01} g_n^{1/2}(J_0)$$

$$\times e^{-hcE_0(v_0,J_0)/kT} g_n^{1/2}(J_0)\omega_{01}\langle J_0 v_0|\mu_{01}(r)|J_1 v_{1j}\rangle\times\cdots \quad \cdots\times\langle J_{2j}v_{2j}|\,\langle J_{2j}M_{2j}|. \tag{6}$$

The $\cdots$ indicates the second half of the symmetric density matrix expression. $|JM\rangle$ are the standard rotational basis functions, $|J_n v_n\rangle$ are the eigenstates of the adiabatic diatomic rovibrational Hamiltonian

$$H_n(r) = \frac{P_r^2}{2\mu} + \frac{J_{ni}(J_{ni}+1)\hbar^2}{2\mu r^2} + V_n(r) \tag{7}$$

with eigenvalues E_n. Consider Eq. (6) in light of a pump–probe sequence, from the center (fourth line) up: An incoherent ensemble, here given by a Boltzmann distribution, with nuclear spin degeneracy $g_n(J_0)$, is pumped by a laser beam centered at ω_{01}. To each transition from V_0 to V_1 corresponds a dipole vector operator $[\mu_{01}(r)\hat{z}\cdot\{\begin{smallmatrix}\hat{Z}\\\hat{X}\end{smallmatrix}\}$, depending on the laser polarization in the $\hat{Z}$ or $\hat{X}$ direction] matrix element and a laser electric field strength (G_{L01}, depending on the offset of the transition frequency from the center frequency ω_{01}). The state then freely propagates for a time τ, after accumulating a phase factor ϕ_{01} during the pump process, which depends on the laser pulse characteristics, and may vary for different eigenstates if the pulse is not transform limited. The same procedure is repeated with a probe pulse, finally yielding a partially coherent superposition of states $|v_2 J_2 M_2\rangle \approx |J_2 M_2\rangle\,|J_2 v_2\rangle$ on V_2. The subscript i indicates columns, the subscript j rows of the density matrix.

Depending on the type of electronic transitions and the laser polarization, the above expression can be greatly simplified. In the case of two parallel electronic transitions probed by laser pulses of the same polarization, $\Delta J = \pm 1$, $\Delta M = 0$. If we also neglect all off-diagonal components of ρ, since they do not contribute to the final trace, and set $t=0$, since the detection process is incoherent and the phase on surface 2 does not contribute,

$$\rho'(\tau) \sim \sum_{\text{all } v\,J} \sum |Jv_2\rangle\langle Jv_2| e^{-i2\pi c[E_1(v_{1i},J\pm 1)-E_1(v_{1j},J\mp 1)]\tau+\Delta\phi_{01}} G_{L12}[E_2(v_2,J)-E_1(v_{1i},J\pm 1)-\omega_{12}]G_{L12}^+[E_2(v_2,J)$$

$$-E_1(v_{1j},J\mp 1)-\omega_{12}]G_{L01}[E_1(v_{1i},J\pm 1)-E_0(v_0,J)-\omega_{01}]G_{L01}^+[E_1(v_{1j},J\mp 1)-E_0(v_0,J)-\omega_{01}]$$

$$\times \mu_{12}(v_2,v_{1i})\mu_{12}^+(v_2,v_{1j})\mu_{01}(v_{1i}v_0)\mu_{01}^+(v_{1j},v_0)\times g_n(J)\omega_{12}^2\omega_{01}^2 e^{-hcE_0(v_0,J)/kT}$$

$$\times \sum_M |JM\rangle\langle JM| J(J+1)\begin{pmatrix}J\pm 1 & J & 1\\ M & -M & 0\end{pmatrix}^2\begin{pmatrix}J\mp 1 & J & 1\\ M & -M & 0\end{pmatrix}^2. \tag{8}$$

The first line shows the time dependence of the coherence itself, the end of the first and second lines weight the rovibrational transitions according to the strength of the laser pulses, the third line contains the contributions of the vibrational transition dipole moments, and the initial incoherent superposition and frequency dependence of the absorption. The sum over M simply becomes the standard J-dependent weight for a parallel two-photon transition in the absence of a perturbing field [e.g., the same factor as in Eq. (4) for the $J+1/J-1$ or $J-1/J+1$ cases]. In the case of two laser beams with perpendicular relative polarization, the last line in Eq. (8) must be replaced by

$$\sum_M |JM\rangle\langle JM|J(J+1)$$

$$\times \begin{pmatrix} J\pm1 & J & 1 \\ M & -M & 0 \end{pmatrix}^2 \begin{pmatrix} J\mp1 & J & 1 \\ M\pm1 & -M\mp1 & 0 \end{pmatrix}^2. \quad (9)$$

The $J\pm1$ and $J\mp1$ are summed *independently* of one another, contributing four terms to the density matrix, as discussed in the previous subsection. We may symbolically write $\rho'(t)$ as

$$\rho'(t) = \sum f_i(J+1)f_j^\dagger(J+1) + \sum f_i(J-1)f_j^\dagger(J-1)$$

$$+ \sum f_i(J+1)f_j^\dagger(J-1) + \sum f_i(J-1)f_j^\dagger(J+1). \quad (10)$$

Two of the terms ($J+1/J+1$ and $J-1/J-1$) contribute mainly to the vibrational coherence when $v_{1i}\neq v_{1j}$, while the remaining ones ($J+1/J-1$ and $J-1/J+1$) contribute

to the rotational coherence when $v_{1i} = v_{1j}$. For example, the last two terms in the case of parallel relative laser polarizations and parallel transitions yield the factor in Eq. (8).

C. Useful simplifications

Expressions such as Eqs. (6) and (8), while rigorous, are not very practical when fitting large sets of data, nor do they yield physical insight into the factors contributing to the transients. At all but the lowest rotational temperatures, the vibrational and rotational contributions (the two pairs of two terms mentioned above) can be separated. Consider first a magic-angle vibrational transient: It may be obtained by proper summing of Eq. (8) (parallel polarization) with Eq. (9) (perpendicular polarization), canceling the $J+1/J-1$ and $J-1/J+1$ terms in Eq. (10). After taking the final trace (dropping unnecessary proportionality constants whenever possible, and the subscript "1" on v since we henceforth consider coherences only on surface 1),

$$I_v(\tau) \sim \sum_J g_n e^{-hcE_{0R}(J)/kT_R} \sum_{i\ j<i} A_{Vij}[J/3\cos(2\pi c\tau[E_v(v_i,J-1)-E_v(v_j,J-1)]+\Delta\varphi_{ij})$$

$$+\frac{J+1}{3}\cos(2\pi c\tau[E_v(v_i,J+1)-E_v(v_j,J+1)]+\Delta\varphi_{ij})]$$

$$\approx \sum_J g_n J e^{-hcE_{0R}(J)/kT_R} \sum_{i\ j<i} A_{Vij}\cos(2\pi c\tau[E_v(v_i,J)-E_v(v_j,J)]+\Delta\varphi_{ij}), \quad (11)$$

where for I_2,

$$E_v(v+1,J)-E_v(v,J)$$

$$=\omega_e - 2\omega_e x_e(v+1) + 3\omega_e y_e(v^2+2v+13/12)$$

$$-\alpha_e J(J+1)+\cdots, \quad (12)$$

and the coefficients $A_{Vij}=A_{Vij}[O(v_2, J),G_{L01},G_{L12},kT, \mu_{01},\cdots]$ include all the information on the detection method, laser profiles, vibrational populations, and transition moments for each pair of rovibrational levels contributing to the transient. The term in Eq. (12) will generally have the largest contribution, particularly for pump and probe pulses with relatively small bandwidth, but $\Delta v=2$ and higher vibrational coherences can also contribute to the transient. It should be noted that there is a rotational contribution, proportional to α_e in the lowest order, which will be seen to have a noticeable effect on even the magic angle vibrational transient.

In parallel detection of a parallel/parallel pump–probe sequence, the rotational transient becomes [$v_{1i}=v_{1j}$ terms in Eq. (8)]

$$I_R(\tau) \sim \sum_{i\ J} A_{Rii} g_n \frac{4J(J+1)}{15(2J+1)} e^{-hcE_{0R}(J)/kT_R}$$

$$\times\cos(2\pi c\tau[E_R(J+1,v_i)-E_R(J-1,v_i)]), \quad (13)$$

where for I_2, $E_R(J,v) = B_v J(J+1) - D_v[J(J+1)]^2+\cdots$. The appearance of the short-time and long-time transients is as shown in Fig. 2, and has been discussed in our previous letter.[5] As for the vibrations, the rotational amplitudes A_{Rii} lump together the intensity, transition dipole and laser profile information, and can be fitted from the data.

It should be noted again that the different time scales and polarized detection almost completely uncouple the rotational and vibrational transients in Eqs. (11) and (13). The remaining effects are (a) in the rotational transient, several peaks appear due to the several vibrations populated in the intermediate electronic state and centrifugal distortion; this has been discussed in detail previously; (b) in the vibrational transient, the rotation–vibration constant α_e has a subtle effect on its envelope and phase: If one were to determine frequencies from the transient by calculating

a power spectrum, this would manifest itself as a broadening and shift in intensity and position of the vibrational peaks, due to their rotational envelope. To see the effect in the time domain, the rotational sum in Eq. (11) (including only $\Delta v = 1$ coherences) is approximated by the integral

$$I_v(\tau) \approx \sum_i A_{Vi,i+1} \int_0^\infty dj\, je^{-hcBj^2/kT_R}$$

$$\times \cos\{2\pi c\tau[\omega_e - \alpha_e j^2 - 2\omega_e x_e(v_i+1) + \cdots] + \Delta\varphi_i\}$$

$$\propto \sum_i A_{Vi,i+1}\{1 + b^2\tau^2\}^{-1}(\cos\{2\pi c\tau[\omega_e$$

$$-2\omega_e x_e(v_i+1) + \cdots] + \Delta\varphi_i\} + b\tau$$

$$\times \sin\{2\pi c\tau[\omega_e - 2\omega_e x_e(v_i+1) + \cdots] + \Delta\varphi_i\}]) \quad (14)$$

where $b = 2\pi\alpha_e kT_R/Bh$ is a temperature dependent scaling factor (here, B is an average rotational constant for the X state of I_2). Equation (14) is an excellent approximation at higher temperatures. It can be seen that if we do not explicitly take rotation–vibration interaction into account by summing over J as well as v, the vibrational coherence is no longer given by a sum of harmonics, but rather by a sum of damped harmonics that phase shift by 90° on a time scale of b^{-1} (≈ 40 ps for I_2 at room temperature). The main effect is a more rapid decrease in vibrational transient intensity than expected for $J = 0$, corresponding to the broadened power spectrum due to the presence of many rotational transitions in a vibrational envelope. A purely vibrational analysis which neglected this fact would yield band origins shifted by approximately $\Delta\omega \approx -\alpha_e kT/Bhc$, leading to a slight reduction in the calculated frequencies.

A similar approximate formula can be obtained for the shape of the rotational transients, and may be useful when $kT > B$, and when centrifugal distortion can be neglected. Taking a single vibrational level with rotational constant B_v from Eq. (13),

$$I_R(\tau) \propto \int_0^\infty dj\, \frac{2}{15}\, je^{-hcB_0 j^2/kT_R}\cos(4\pi c\tau B_v j)$$

$$\propto L_{1/2}^{-1/2}(b'^2\tau^2)e^{-b'^2\tau^2}$$

$$\propto (1 - b'^2\tau^2)e^{-b'^2\tau^2} \quad (15)$$

is the rotational transient in parallel detection near time 0 or measured from the center of a full recurrence. The quadratic approximation to the generalized Laguerre function $L_{1/2}^{-1/2}$ is a good approximation wherever $I_R(\tau)$ substantially differs from zero. The scaling factor b' equals $4\pi c B_v(kT_R/B_0 hc)^{1/2}$.

D. Conversion from the time to the frequency domain

As discussed in Ref. 5, the best way of obtaining rotational constants is a direct fit to Eq. (13). This is due to the fact that centrifugal distortion cannot be neglected and results in a "ringing" pattern after the rotational peaks. Since the ultrafast pump pulse generally covers only a few vibrational levels at a time, producing only a few oscilla-

tions in I_R, this method is reliable even when all coefficients A_{Rii} are fitted individually.

Vibrational constants could be determined using Eqs. (11) or (14). At a first glance, a nonlinear fit to Eq. (11) or (14) seems impractical, unless the frequencies are known fairly accurately to begin with, due to the large number of parameters that must be fitted. A more straightforward way would be the determination of the power spectrum of the early time transient in Fig. 2(a). In two earlier letters, we have applied both FFT and maximum entropy algorithms to the determination of power spectra;[5,6] before discussing application to I_2, we briefly apply them, as well as Prony's spectral method[17] and nonlinear fitting, to a test model.

Figure 5(a) shows a plot of a synthetic transient generated from three harmonics, without damping or phase distortion, as well as the "exact" power spectrum (if the transient had been extended to infinite times), which is the information we in principle desire. Consider now the four models we have tested.

At a first glance, Prony's spectral method, which is designed to extract frequencies from a time series due to exponentially damped harmonics, appears like an ideal choice.[17] When the frequencies to be extracted are close to one another, as is the case here, we found this to be true only for very high signal-to-noise ratios. At low S/N ratios, Prony's method fails. The reason for this lies in the manner in which it attempts to decouple the harmonic amplitudes from the frequencies, determining the latter by first solving a linear set of equations, then determining the former with the frequencies held fixed in another linear least squares fit. In effect, Prony's method has a short temporal correlation length, but when two frequencies are close together, their distinguishability requires the recognition of very slow changes in the amplitude envelope of a transient. In practice, the method can be made to converge by a careful choice of the equations to be included in the least-squares fit, but is not suitable for an "automated" determination of frequencies.

Fast Fourier transform (FFT) and the maximum entropy method (MEM) fare considerably better. The power spectra and transients derived from them are shown in Fig. 5. The results are symptomatic of the performance of these techniques.

FFT assumes a periodic continuation of the function, expanded in harmonics which are multiples of a single fundamental frequency. This is clearly not a perfect model for Eq. (11), since the frequency components are better described as the sum a constant fundamental frequency and a (nearly) linearly increasing offset, at least in the present case. The result is an unnecessary broadening of lines due to spectral leakage, as well as a resolution limited by the sampling frequency (Nyquist limit). On the other hand, the amplitudes of the components are quite well represented.

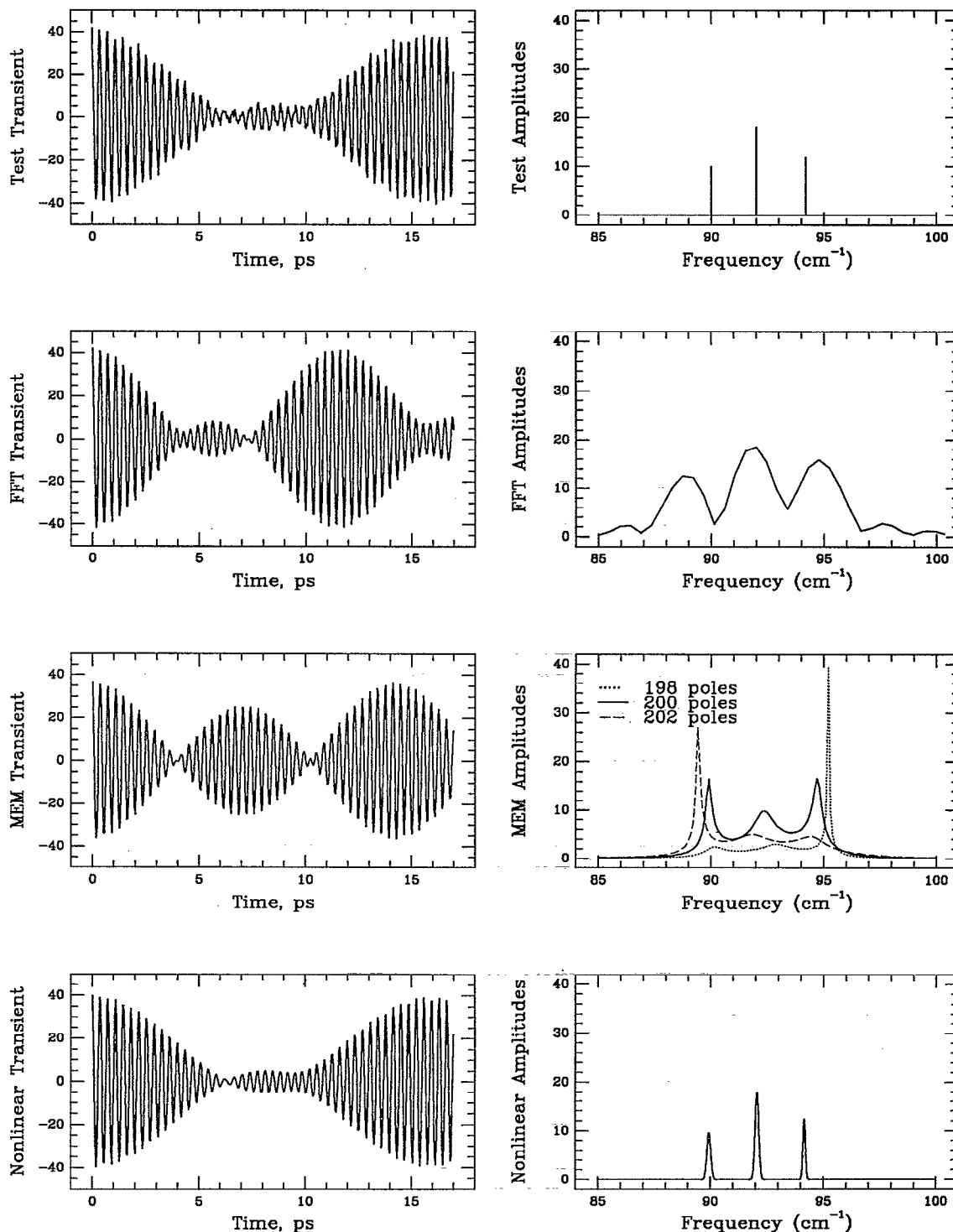Burg's MEM (see Ref. 17) assumes a maximally ran-

FIG. 5. Comparison of different methods for extracting frequency components from a temporal transient. The top row shows a test transient (no rotational effects) and the ideal power spectrum if the transient were noise free and extended to infinite times; the second row shows a fast Fourier amplitude spectrum and the transient generated from it; the third row shows a maximum entropy amplitude spectrum and its transient; note the sensitivity to pole number discussed in the text; the bottom row shows an amplitude spectrum extracted by the nonlinear fitting procedure described in the text, and the resulting temporal transient. The widths of the nonlinearly fitted peaks are the 2σ precision of the nonlinear fit.

dom continuation of the function beyond the sampled region, representing the power spectrum by a denominator Padé expansion well suited for sharp peaks (due to the presence of poles in the analytic continuation of the Padé approximant). This model is also imperfect. In the case of noisy transients at nearby frequencies, it leads to highly inaccurate amplitudes, and fluctuations in the frequencies as a function of the number of poles included. In the case

on hand, there is no "objective" reliable way of determining the number of poles in the expansion; as an approximate guide, the frequencies and peak amplitudes generally stabilize, while the peaks narrow, near the optimal number of poles (but the opposite may happen, at least if optimal is meant to indicate the smallest deviation from the correct frequencies); the resulting frequency rms error, 0.6 cm^{-1}, is quite comparable to the error of the FFT spectrum, 0.75 cm^{-1} (close to the Nyquist step size).

For the present application, the general conclusions are as follows:

(1) FFT provides superior amplitudes;

(2) FFT and MEM provide comparable frequency accuracy with noisy spectra (MEM becomes increasingly better as the S/N improves, since it is not hampered by the Nyquist limit);

(3) MEM provides superior peak identification, due to the narrower line widths.

Finally, we turn to nonlinear fitting methods. While it is not possible to nonlinearly fit a noisy transient directly, the following series of steps has been found to yield a very robust, reliable and automated means of determining frequency components without any *a priori* knowledge of their exact positions or amplitudes:

(1) Determine an approximate power spectrum by FFT or MEM;

(2) Use a peak finding routine to locate the strongest peaks;

(3) Fit the positions to a smooth model that approximately represents the system Hamiltonian (e.g., in the case of I_2, $\omega_i = \omega_0 + \Delta_1 \omega i + \Delta_2 \omega i^2$, where i is an index offset from the vibrational quantum number by an unknown amount; if $i = 0$ is chosen for the lowest frequency peak, ω_0 represents the first vibrational frequency in the line cluster, and $\Delta_1 \omega \approx -2\omega_e x_e$);

(4) Fit intensities to a simple harmonic model by *linear* least squares: $I(t) = \Sigma A_i \cos(\omega_i t) + B_i \times \sin(\omega_i t)$;

(5) Relax all parameters in a nonlinear fit to a more accurate model, such as Eqs. (11) or (14).

The result of such a fit, implemented in a single program RECFIT, is shown in Figs. 5(g)–5(h), yielding by far the most precise frequencies and amplitudes, with a correspondingly longer processing time. The precision obtained by this method in the test case is 0.005 cm^{-1}, or 10 ppm. The nonlinear fit model is thus capable of extracting frequencies with a precision well in excess of the Nyquist limit, with $\Delta \nu$ less than $1/2t_{\text{scan}}$ by 2 orders of magnitude in the best cases. It should be noted that this by no means represents a violation of the time-frequency uncertainty principle, which would dictate $\Delta \nu \sim 1/\Delta t$ for measured frequency and temporal quantities: the frequencies reported here are fitted, not observed values, their precision being due to the choice of a fitting model better than FFT, and assumed *a priori* to represent the data. Whether the frequencies are accurate in addition to being precise depends on the goodness of the model chosen, but since the Dunham Hamiltonian is known to represent I_2 energy levels to
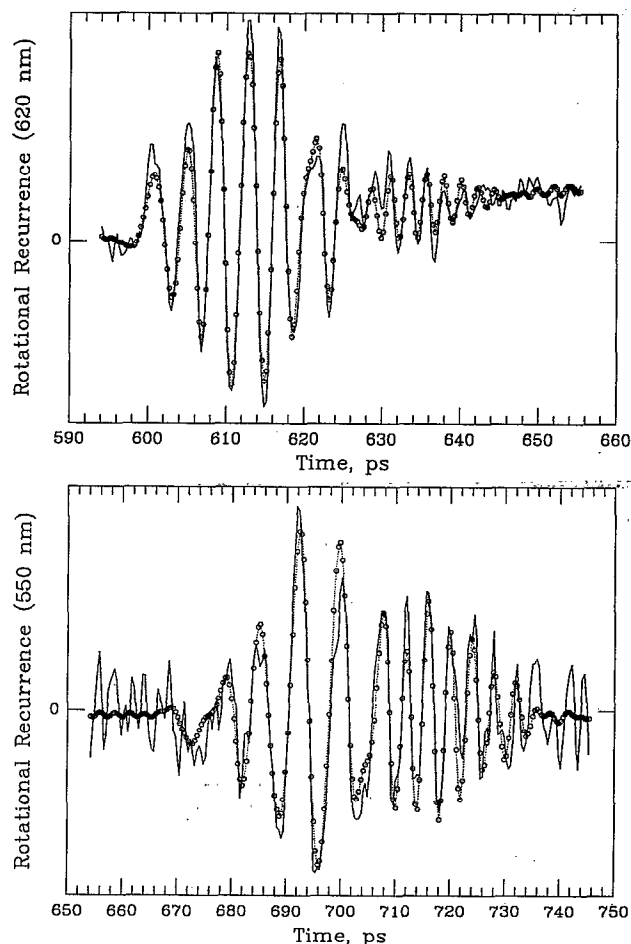

FIG. 6. Experimental full rotational recurrence at 620 nm ($v \approx 9$) and 550 nm ($v \approx 25$), detected with parallel laser polarization (solid line), and fit to Eq. (13) (dotted line and circles).

high accuracy, the frequencies obtained here will also be accurate. The analogy from high-resolution spectroscopy would be a determination of a band origin to better than the linewidth, by fitting an entire rovibrational band to a model Hamiltonian known to hold for the molecule under investigation. We will see in the following how these results carry over to real temporal data.

IV. APPLICATION: I_2

A. Rotational transients

We now consider the application to the rovibrational coherence of a real system, I_2 in the B electronic state. Figure 6 shows as examples rotational transients obtained by pumping at 620 nm ($v \sim 9$), and 550 nm ($v \sim 25$), together with fits to Eq. (13). Inclusion of rotational intensity alternations and individual adjustment of vibrational level amplitudes has yielded a slight improvement over the fits in Ref. 5. The rotational constants for these particular levels are shown in Table I, together with precise high-resolution values. The small differences, as well as methods for assigning vibrational quantum numbers, will be discussed together with the vibrational frequency determina-

TABLE I. Comparison of FWS and accurate high resolution vibrational frequencies and rotational constants (in cm^{-1}).

Vibrational parameters Wavelength	vl^a	vu	Frequency	Ref. 7	Ratio
620 nm	10	11	107.908	107.912	1.000 04
	9	10	109.598	109.631	1.000 30
	8	9	111.278	111.327	1.000 44
	7	8	112.957	113.002	1.000 38
	6	7	114.637	114.657	1.000 17
550 nm	27	28	75.440	75.421	0.999 75
	26	27	77.500	77.483	0.999 78
	25	26	79.470	79.531	1.000 77
	24	25	81.430	81.563	1.001 63
					⟨1.000 40⟩

Rotational constants Wavelength	v^a	$B(v)$	Ref. 7
620 nm	6	0.027 97	0.027 98
	7	0.027 80	0.027 81
	8	0.027 62	0.027 64
	9	0.027 45	0.027 46
	10	0.027 27	0.027 29
	11	0.027 08	0.027 11
550 nm	23	0.024 58	0.024 62
	24	0.024 34	0.024 38
	25	0.024 14	0.024 14
	26	0.023 89	0.023 89

$^a vl$ and vu are the vibrational levels assigned to a specific frequency component of a transient, v is the vibrational quantum number assigned to a specific observed rotational recurrence peak.

tions. Here we just note that as before, centrifugal distortion (now up to third order) and a finite rotational temperature (~ 380 K) had to be included to account for the observations.

This can be circumvented by the use of a molecular beam, but paradoxically, at a drastic loss in energy resolution. Figure 7 shows a rotational half-recurrence obtained
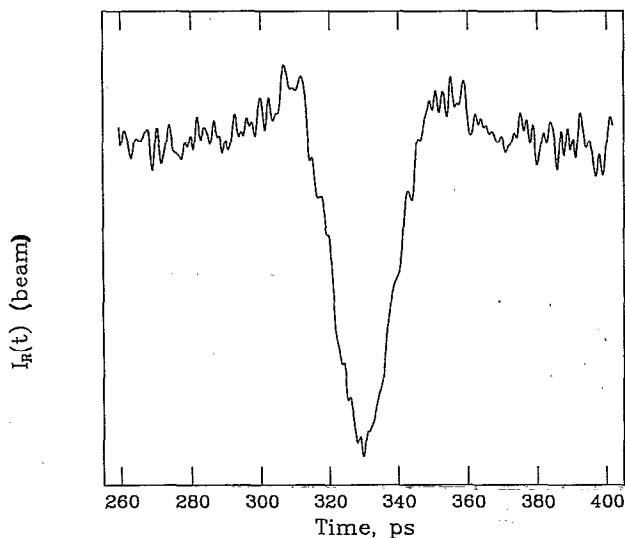
FIG. 7. Rotational half recurrence in a molecular beam [see M. Dantus, M. H. M. Janssen, and A. H. Zewail, Chem. Phys. Lett. **181**, 281 (1991)].
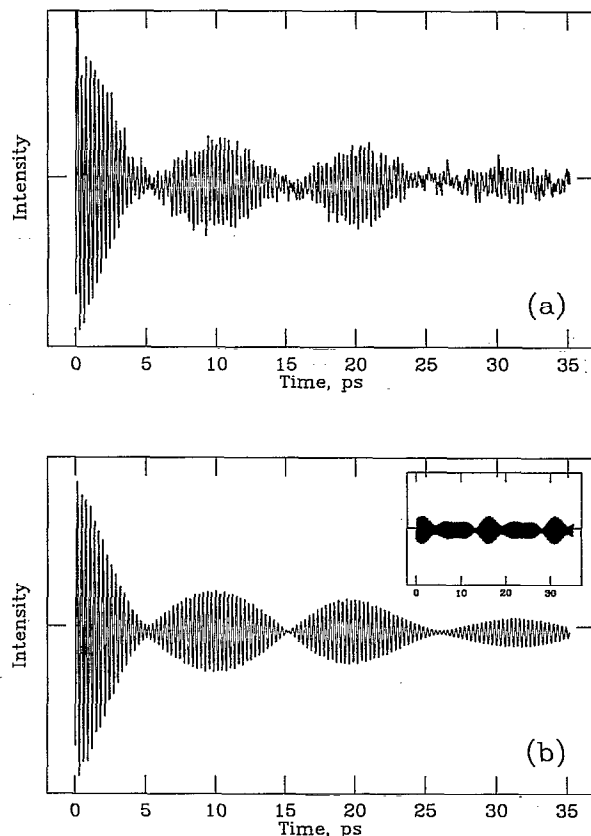
FIG. 8. (a) Magic-angle vibrational transient at a pump wavelength of 620 nm ($v \approx 9$); (b) optimal fit to Eq. (14), with rotation–vibration interactions included in the amplitude damping and a nonlinear phase shift; the insert shows the best fit without taking rotation into account, i.e., to a sum of vibrational harmonics; six vibrational states were required to reproduce the experimental observations.

at $\lambda_{pump} = 560$ nm. The rotational recurrence now has the simple appearance expected at low temperatures,[10] without the "centrifugal distortion tail." Unfortunately, the width has increased to obscure the vibrational structure. Without knowing the laser bandwidth and temperature of the molecular beam, and at realistic signal-to-noise ratios, the number of vibrations covered and the α_e value cannot be properly decorrelated, making specific vibrational assignments impossible. As seen below, the vibrational frequencies are also better determined at higher temperatures, although for entirely different reasons.

B. Vibrational transients

Figure 8(a) shows an experimental magic angle vibrational coherence at 620 nm near room temperature ($v \approx 23$–27). Figure 9 shows the corresponding power spectra obtained by the FFT, MEM, and nonlinear fitting methods. As in the test case discussed above, FFT and MEM power spectra (with optimally adjusted phase information added) cannot reproduce the experimental transient even in its gross features. Instead, Fig. 8(b) shows transients calculated from two different nonlinear fits. The insert assumes that $b = 0$ in Eq. (14), i.e., neglects the rotation–
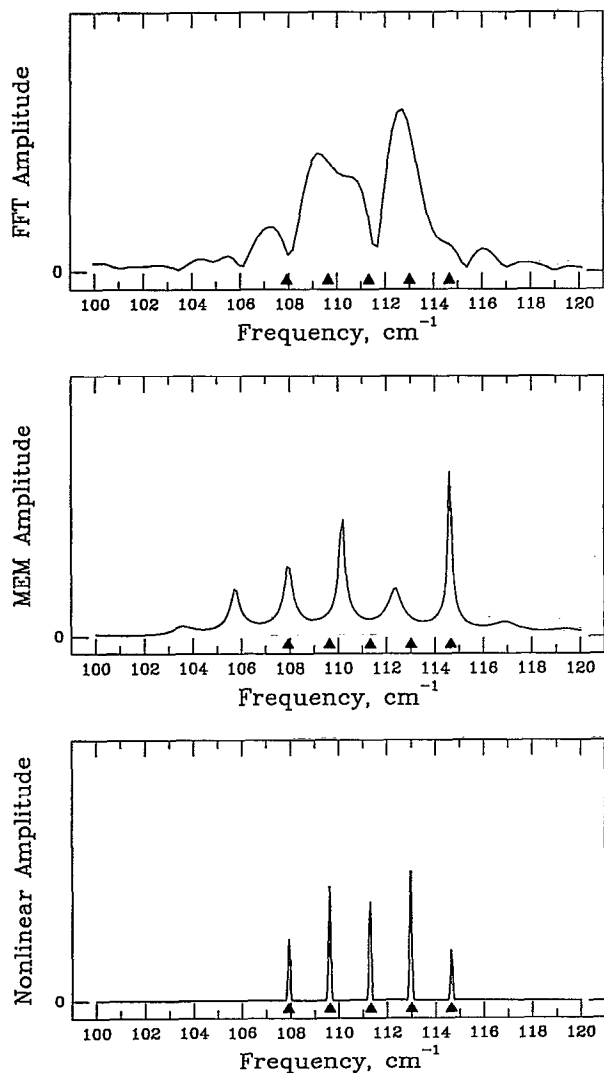
FIG. 9. Amplitude spectra corresponding to the 620 nm transient in Fig. 8; the top figure shows the FFT result (mean deviation 0.7 cm^{-1}); the middle the MEM vibrational peaks (mean deviation 1.2 cm^{-1}); the bottom the nonlinear fit results (mean deviation 0.02 cm^{-1}); the actual vibrational frequencies, as obtained from cw spectroscopy, are indicated by black triangles; as noted in the text, the broader peaks of the FFT do not necessarily indicate lower accuracy than obtained by the MEM method, and the FFT also reproduces the actual amplitudes somewhat better. The widths of the nonlinearly fitted peaks are the 2σ precision of the nonlinear fit.
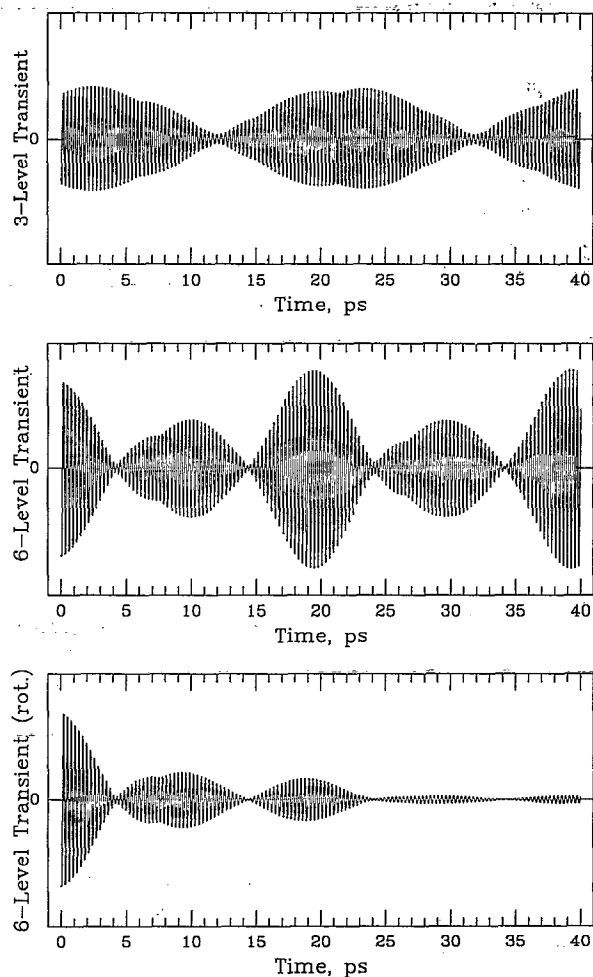

FIG. 10. Effect of multilevel interference on the transient; the top figure shows a three-level transient near $v=9$; the recurrence occurs at $t=1/(2c\omega x)$, as expected; the middle figure shows the full six-level transient, without rotational effect; a vibrational half-recurrence is observed due to intensity alternation of the vibrational amplitudes; the bottom shows the same transient including the rotational damping effect.

vibration interaction. The main plot shows the result of freely varying b, and reproduces the observed transient within the experimental noise, yielding a value of b close to that expected. The vibrational frequencies obtained from the two fits agree to about 0.01 cm^{-1}. Note that for simplicity's sake, we show the calculated vibrational frequencies of the levels needed to converge the nonlinear fit, rather than the local values of ω_0, $\Delta_1\omega$, $\Delta_2\omega$, etc., fitted as described in the previous section. [See the following section on assignment of quantum numbers and how to obtain $\omega(v)$ from ω_0, $\Delta_1\omega$, etc.] At most two anharmonic con-

stants (up to $\Delta_2\omega$) were required to satisfactorily reproduce any of our transients.

One interesting feature in the 620 nm vibrational transient is the partial recurrence at 10 ps. This is only one-half the time expected from a simple anharmonic three-level picture of I_2 at $v=25$. Figure 10 shows three partial simulations of the 620 nm transient: At the top, only the three strongest amplitudes from the fit to Eq. (14) are included, and a full vibrational recurrence is observed at 20 ps. If three more vibrational amplitudes are added, the middle transient is obtained, which shows a strong partial vibrational recurrence, due to alternating vibrational amplitudes (due to FC factors). At the bottom of Fig. 10, the rotation–vibration interaction has been included, and the transient now strongly resembles the exact result of Fig. 8. Clearly, the maxima in the transient cannot always be straightforwardly "inverted" to the anharmonicity of the vibrational levels.

Another cell transient obtained at 550 nm ($v\approx25$) and the corresponding best fit are shown in Fig. 11, yielding
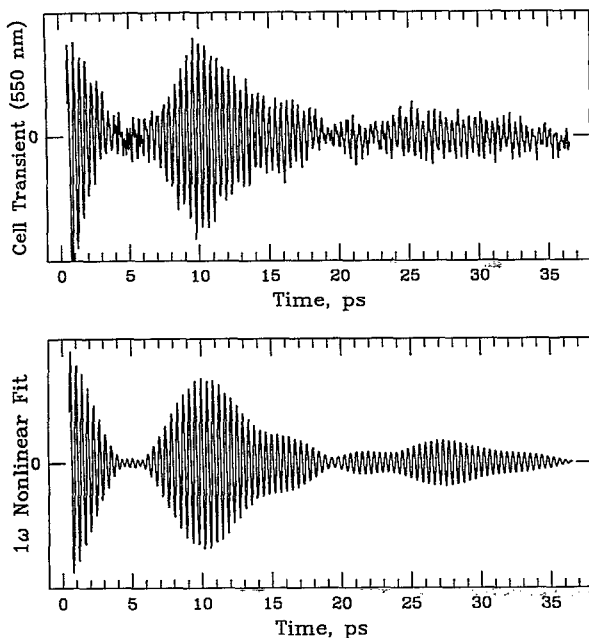
FIG. 11. Vibrational transient at 550 nm and room temperature; the nonlinear fit very nearly reproduces the experimental data, although only nearest-neighbor vibrational coherences are included, just as in Fig. 9.

similarly good agreement. Here the fit is to a parallel laser polarization vibrational transient, with the rotational anisotropy removed by fitting and subtraction.

The vibrational frequencies from the best fit are shown in Table I for the two transients. A conversion factor of 0.3951 fs/step was used in converting the motion of the translation stage used in the experiments from the distance to the time domain. Comparing to the fractional error with exact high-resolution measurements, it can be seen that the fitted vibrational frequencies show a small systematic deviation. Indeed, the deviation is smaller than one might expect from the calibration error. Since it appears in a number of entirely separate transients, it is probably safe to assume that the residual error of 0.04% is due to calibration. The accuracy in Table I, 0.03 cm^{-1}, could thus be improved to 0.01 cm^{-1} with an interferometrically calibrated translation stage, yielding an accuracy comparable to cw experiments, and 10–50 times better than expected from Fourier transform techniques ($1/2t_{scan} \approx 0.6$ cm^{-1}). The fairly good agreement of the 550 nm data further demonstrates that nearly the same accuracy can be obtained from artificial magic-angle transients as from true magic angle scans. In general, we find that the nonlinear fitting method outperforms the Nyquist limit by a factor of typically 10 or more for the best signal-to-noise ratio scans (S/N > 15), and reduces to performing near the Nyquist limit for transients with a signal-to-noise ratio below 2:1.

Fits to Eq. (11) instead of Eq. (14) produce very similar results, but require more computer time, due to the extended rotational summations needed at higher temperatures. We also considered fits including $(v+1/2)^2 J(J+1)$ and $(v+1/2)J^2(J+1)^2$ rotation–vibration terms in
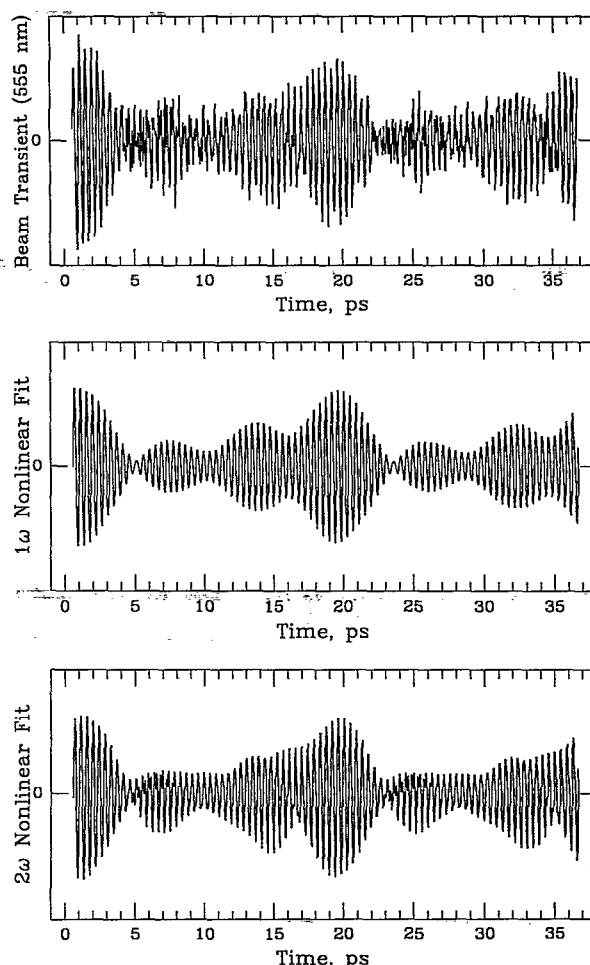

FIG. 12. Top: molecular beam transient at 555 nm; middle: nonlinear fit, including only nearest-neighbor vibrational coherences; it has the same general envelope, but fails to account for higher frequency beat and a pronounced asymmetry of the transient; bottom: nonlinear fit, including also next-nearest-neighbor interactions; the asymmetric envelope seen in the experiment is reproduced, as well as the most pronounced higher frequency beats.

addition to the $(v+1/2)J(J+1)$ term, but found them to yield no significant improvement. Even at higher temperatures, their effect on the frequencies should remain small, as even letting $b=0$ was found to have a more pronounced effect on the transient envelope than the constituent frequencies.

Figure 12 (top) shows a transient obtained at $\lambda_{pump} = 555$ nm in a molecular beam expansion, showing a fundamental frequency very similar to that in Fig. 11(a), but generally more complex structure. The room temperature transients discussed above were fitted including only the nearest-neighbor term of Eq. (12). Such a fit, with freely varying b, is shown in Fig. 12 (middle). As expected, b is an order of magnitude smaller than for the room temperature transients. However, the symmetric transient obtained from nearest neighbor coherences matches the experimental one only in its general features.

Figure 12 (bottom) shows a fit to the beam data including second-nearest neighbor coherences of frequency
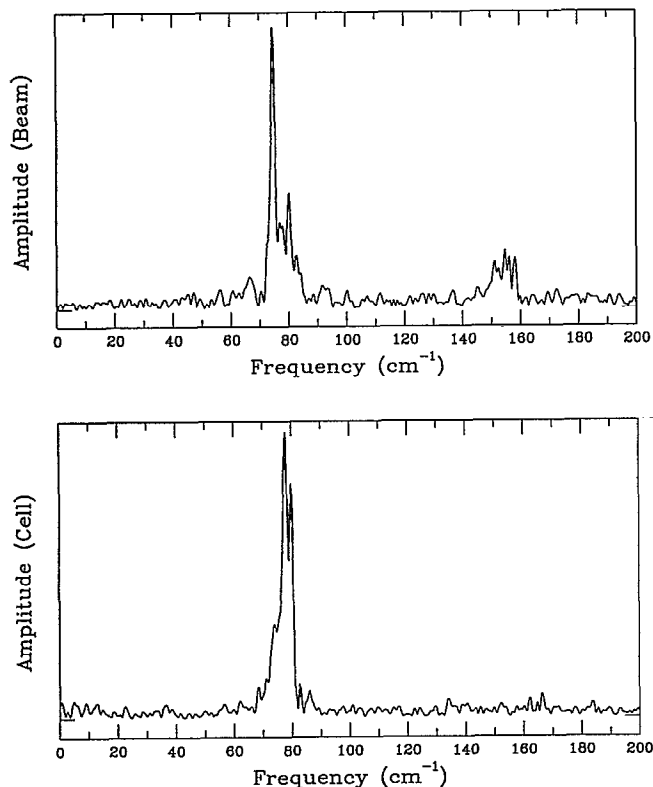
FIG. 13. Amplitude spectra of the beam transient at 555 nm and the room temperature transient at 550 nm; the molecular beam transient shows a strong 2ω component which has not been averaged away by vibrational and rotational excitation of the initial density matrix (see the text).
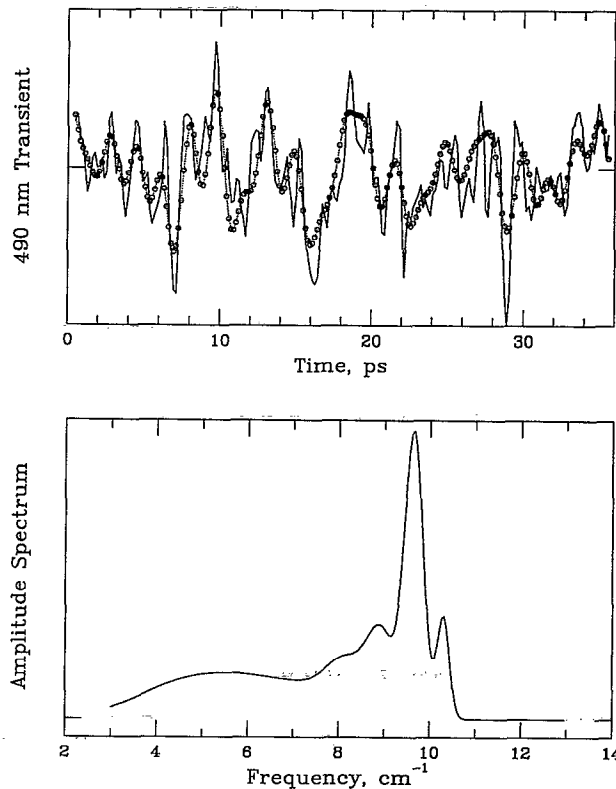
FIG. 14. Fit to a very noisy transient pumped at $\lambda = 490$ nm, which lies mostly above the dissociation threshold; a sharp initial peak corresponding to dissociating I_2 molecules is not shown and fitted; the fit reproduces the general structure of the transient, but as components higher than 2ω were not included, it cannot reproduce the sharper features in the transient.

$\approx 2\omega$. It reproduces very well the asymmetry of the observed transients, and some of the 2ω beats, and yields similar frequencies. This is, however, at the expense of a much larger set of nonlinear fitting parameters (all the amplitudes and phases for the 2ω components). In effect, raising the temperature symmetrizes and simplifies the structure of the transient due to rotational and vibrational averaging, while preserving the desired information about the 1ω components with the same accuracy. Here, as opposed to the rotational coherences, it is a smoothing of the transient at higher temperatures that leads to a faster and simpler extraction of vibrational frequencies. Figure 13 shows Fourier amplitude spectra of the ~ 550 nm transients in Figs. 11 and 12. The beam transient shows a much larger 2ω component. From the above discussion, it is clear that its size is not solely due to the laser response time, but also due to incoherent vibrational and rotational averaging at higher temperatures, which actually results in simpler coherence decays.

Finally, Fig. 14 shows the results that can be extracted from a very noisy transient, as a worst-case scenario for the nonlinear fitting technique. The vibrational frequencies extracted with the smallest uncertainty are 10.3(7) and 9.6(7) cm^{-1}, and could be assigned by extrapolating from the next smallest set near 15 cm^{-1} (see below). A number of other vibrational frequencies down to 4.3 cm^{-1} were

also determined in the fit, but could not be assigned reliably due to the large uncertainty in the frequencies. This shows that meaningful results can still be extracted from noisy transients, with a concomitant loss in the accuracy of the information.

V. INVERSION TO THE POTENTIAL

In this section, we consider inversion of the data obtained above to the potential function (PF). Since this is closely related to the process of vibrational assignments, we also discuss this issue here.

A. Vibrational assignments

In cw spectroscopy, one is faced with the task of assigning specific lines to a complete set of quantum numbers. The wave packet approach does not bypass this problem. While the above analysis directly yields a spectrum of rotational constants B_v and rotationless band origins ν_v, a vibrational quantum number (and in general, several other quantum numbers) must still be assigned to the dual spectra. In the ideal case, assigning the rotational and vibrational constants to specific v values is an easy task. Consider Fig. 15, showing the pure vibrational progressions obtained from the analysis is Sec. IV. As one approaches
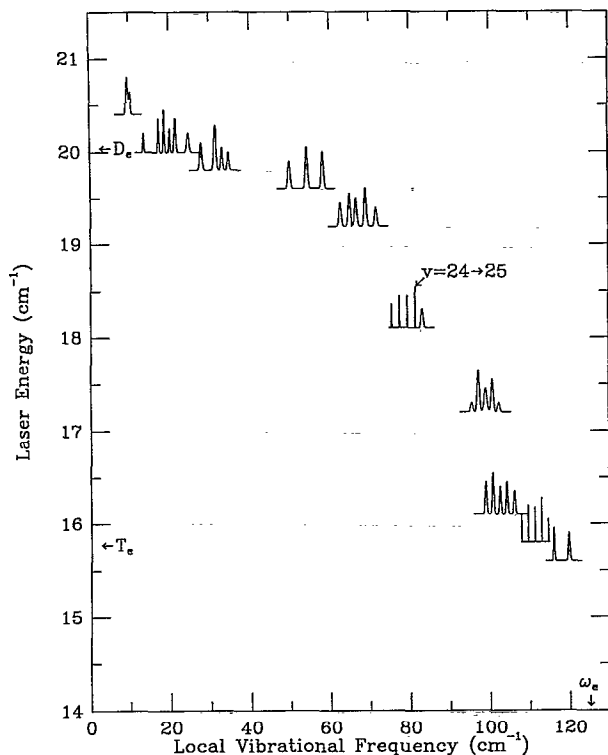
FIG. 15. Vibrational progression in the B state of I_2 as measured by FWS: the curves are the amplitude spectra obtained from nonlinear fits to the experimental transients; the widths correspond to the estimated uncertainties; due to Franck–Condon factors and thermal excitation, the term energy and dissociation limit indicated by arrows do not perfectly line up with the laser energy.

FIG. 16. High resolution and temporally derived RKR curves for the B state of I_2.

the dissociation limit, the vibrational peaks crowd together as expected from higher order anharmonicity effects.

If the Franck–Condon factors are favorable, this progression can be followed to lower wavelengths, until the "first" vibrational peak is found, which can be assigned to $v=0$. Vibrations are then successively numbered up the ladder; a few missing rungs are not important, since only one assignment will generally bridge the gap without yielding grossly fluctuating local anharmonicity constants. In practice, the relative numbering is seldom a problem, but finding the $v=0$ peak can be. For instance, in I_2 at room temperature, the transitions terminating below $v=4$ in the B state are too weak to be detectable. Fortunately, vibrational transitions up to near dissociation are accessible, which constrains the vibrational level positions sufficiently to allow only one unique fit to a power series in $v+1/2$ without unduly large or fluctuating higher order terms in the Dunham expansion of the vibrational and rotational spectra.

The rotational assignment is usually possible in the same manner by working up a rotational ladder. In cases where the B_0 peak is not accessible, comparing peak intensities with the vibrational transient allows a unique assignment by a somewhat more detailed consideration of the factors A_{Vij} and A_{Rii} mentioned in Sec. III. As can be seen
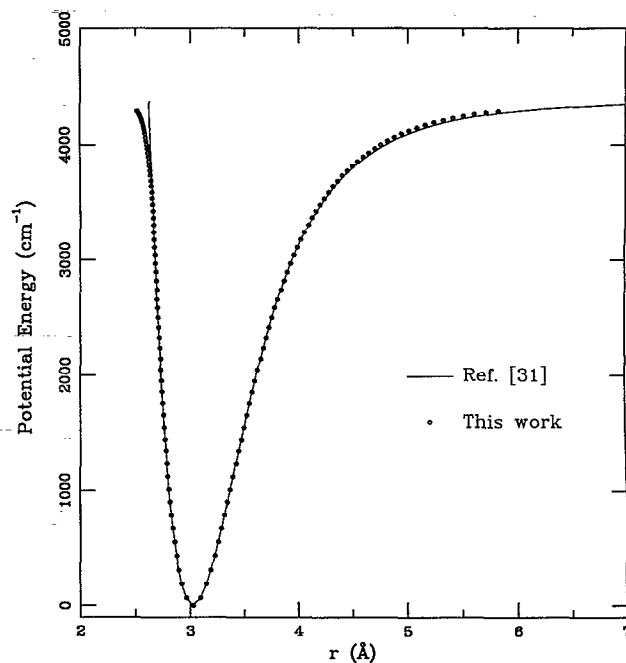
from Eqs. (2) and (8), the A_{Vij} can be written as a product $c_i c_j$, while the A_{Rii} can be written as products $c_i'^2$; if the $J\pm1$ splitting is not too large compared to the laser bandwidth, $c_i' \approx c_i$, strongly correlating vibrational and rotational amplitudes.

Note that in principle one could also use a fit to the c_i to determine the Franck–Condon factors between the two surfaces directly. The nearest neighbor and higher order amplitudes $A_{Vi,i+1}$, $A_{Vi,i+2}$ $\cdots$ overdetermine the c_i, yet in practice, the higher coherences are strongly damped by the laser bandwidth, which must be known accurately, and most importantly, the effects of rotation-vibration interaction; as a result, the c_i cannot be fitted accurately except when the signal to noise ratio is very high and the excitation profile is well characterized.

B. Potential functions

A number of standard inversion procedures can be used once the vibrational frequencies and rotational constants have been determined. Table II summarizes the results of the measurements (including some older measurements from our previous work[5]), and the Dunham coefficients fitted to reproduce those measurements over the entire range of vibrational quantum numbers covered. We here briefly consider the RKR inversion[18] and fitting to parameterized PFs[19] as two methods of extracting the potential function from temporally obtained data.

Figure 16 summarizes the results for the I_2 PF obtained by RKR inversion; the error in the absolute energies

TABLE II. Fitted Dunham expansion parameters; Uncertainties in parentheses are two standard deviations.

Dunham coefficients in cm^{-1}		Observed and calculated rotational constants (in cm^{-1})		
		v	$B(v)$ (e. u.)	B (calc.)[a]
$Y_{00}=$	0.153 29(calc.)	6	0.027 97(0.000 02)	0.027 969 7
$Y_{10}=$	126.07(25)	7	0.027 80(0.000 02)	0.027 799 3
$Y_{20}=$	−0.825(35)	8	0.027 62(0.000 02)	0.027 625 3
$Y_{30}=$	0.002 584(2 271)	9	0.027 45(0.000 02)	0.027 447 5
$Y_{40}=$	−0.000 225 5(692)	10	0.027 27(0.000 02)	0.027 266 1
$Y_{50}=$	0.000 003 559(959)	11	0.027 08(0.000 02)	0.027 081 1
$Y_{60}=$	−0.000 000 015 95(490)	22	0.024 81(0.000 02)	0.024 811 1
$Y_{01}=$	0.028 986 (107)	23	0.024 58(0.000 02)	0.024 583 9
$Y_{11}=$	−0.000 143 9(222)	24	0.024 34(0.000 02)	0.024 353 3
$Y_{21}=$	−0.000 001 918 9(13 787)	25	0.024 14(0.000 02)	0.024 119 3
$Y_{31}=$	0.000 000 003 176(26 718)	26	0.023 89(0.000 02)	0.023 882 0
		27	0.023 63(0.000 02)	0.023 641 4

Observed and calculated vibrational frequencies (in cm^{-1})

vl	vu	Freq. (e. u.)	Freq. (calc.)[a]
3	4	119.790(0.300)	119.539
5	6	116.000(0.200)	116.272
6	7	114.637(0.020)	114.625
7	8	112.957(0.020)	112.966
8	9	111.278(0.020)	111.292
9	10	109.598(0.020)	109.601
10	11	107.908(0.020)	107.890
11	12	106.200(0.300)	106.159
12	13	104.300(0.300)	104.406
13	14	102.600(0.300)	102.629
14	15	100.800(0.300)	100.830
15	16	99.000(0.300)	99.006
23	24	83.200(0.400)	83.574
24	25	81.430(0.070)	81.553
25	26	79.470(0.070)	79.515
26	27	77.500(0.070)	77.462
27	28	75.440(0.070)	75.397
29	30	71.600(0.400)	71.237
30	31	69.000(0.400)	69.146
31	32	66.600(0.400)	67.051
33	34	62.700(0.400)	62.858
32	33	65.000(0.400)	64.954
35	36	58.400(0.400)	58.677
37	38	54.400(0.400)	54.529
39	40	50.000(0.400)	50.433
47	48	34.900(0.300)	34.964
48	49	33.300(0.300)	33.171
49	50	31.600(0.400)	31.415
51	52	28.100(0.400)	28.023
53	54	24.900(0.400)	24.800
55	56	21.700(0.300)	21.755
56	57	20.300(0.200)	20.301
57	58	18.900(0.200)	18.893
58	59	17.500(0.200)	17.531
61	62	13.700(0.200)	13.722
64	65	10.300(0.200)	10.312
65	66	9.600(0.700)	9.258

[a] e. u. is the estimated 2 sigma uncertainty; vl and vu are the lower and upper vibrational quantum numbers fitted to a specific frequency component of a transient.

(measured from the bottom of the B-state well), amounts to 3 cm^{-1} at $v=65$, 65 cm^{-1} below the dissociation limit. The error in the turning point difference, $r_{outer}-r_{inner}$, is similarly small up to $v=70$. The actual turning points tend to shift increasingly to smaller internuclear distances above $v=50$, due to the lack of rotational sampling above $v=30$.

A number of methods can circumvent this artifact of the RKR inversion. One that also yields a continuously defined potential involves fitting the rotational constants and vibrational frequencies directly to a model potential; a

TABLE III. f potential parameters for the B state of I_2; Values of p's and q's are such that r is in Angstroms (see the text).

D	4381.5 cm^{-1}
p_0	1.0
p_2	−2.0
p_4	0.685 292 08
q_2	7.9
q_4	−8.242 915 8
q_6	1.981 569 2
q_8	0.245 251 51
q_{10}	0.061 353 379
q_{12}	−0.108 471

particularly convenient function is the "f potential" of Ref. 19,

$$V(r) = D[1 - f(r)]^2 \qquad (16a)$$

which fits the data to a smoothly and monotonically decreasing mapping function; the following Padé approximant for f was found sufficient in this case,

$$f(r)$$

$$= \frac{p_0 + p_2 r + p_4 r^2}{q_1 r^{1/2} + q_2 r + q_4 r^2 + q_6 r^3 + q_8 r^4 + q_{10} r^5 + q_{12} r^6 + q_{14} r^7},$$
$$(16b)$$

where r is the internuclear distance. If we constrain two of the coefficients to be

$$q_1 = 2.9343 \times 10^{-3} (D/Z)^2 p_0 \quad \text{and} \quad q_{14} = 2D/C_5 p_4,$$
$$(17)$$

where D is the dissociation energy in cm^{-1}, Z the nuclear charge (127), and C_5 the van der Waals coefficient (3.11 $\times 10^5$ cm^{-1} Å^5) for the B state of I_2, then the PF will have the correct $1/r^5$ behavior at large internuclear distances,[20] and the correct (shielded) Coulombic behavior at small r. The resulting fitted constants q_i and p_i are shown in Table III, and the potentials are compared in Fig. 17. Much better behavior is found for the f-potential near the dissociation limit, yielding a continuous global potential function with only a few adjustable parameters.

VI. COMPARISON WITH CLASSICAL AND QUANTUM DYNAMICS

The classical treatment of the temporal data and their inversion to the potential have been discussed by Bernstein and Zewail.[6] Basically, the local period can be related to the difference in the turning points of the potential. At all wavelengths, experiments and classical calculations agree. However, the classical treatment does not give as precise information as the quantum calculation because of structure in the wave packet.

In our previous letter, we reported a time-dependent wave packet calculation on the RKR potential obtained therein.[5] Engel and Metiu reported calculation on model surfaces of the E state in addition to the f state.[21] In our calculations, it was shown that the RKR potential yielded simulated vibrational transients which in turn had vibra-
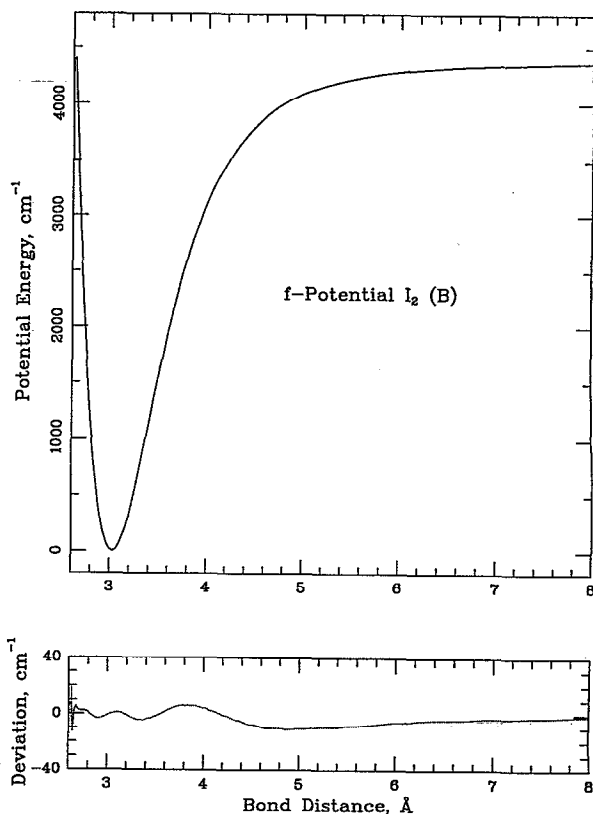

FIG. 17. f potential for I_2 derived from the present data, and difference potential to the RKR potential from Ref. 31.

tional frequency components very close to those determined in the experiment.

Here our goal is not to demonstrate self-consistency again, which can be assumed to hold better now than in the earlier potential determination, since the actual observed transients can be simulated within experimental uncertainty. Rather, we perform a series of pump–probe calculations on simple, approximate Morse-model potentials for the X, B, and f states, to investigate the general effects of vibrational and rotational excitation in the X state on the transients. The goal is to see whether the trends ascribed to the various room temperature and molecular beam experiments for the coherence transients are indeed borne out by theoretical simulations.

We consider only total fluorescence from the f state. This greatly simplifies the calculations, since only the amplitude of the final wave packet need be considered, rather than a weighted sum of the type shown in Eq. (5). In the experiments described in Ref. 8, the E state should not play a great role, since fluorescence in the experiments was detected only near 340 nm, which can result only from the f state directly, or via collisional quenching from it to the D' state.

The time-dependent quantum formalism, discussed by Kosloff and Hammerich,[22] Williams and Imre,[23] Engel and Metiu,[24] Hartke and Manz,[25] and others[22] has been applied by us previously to I_2 (Ref. 5) and several other molecules,[26] and need not be rederived here in detail. The
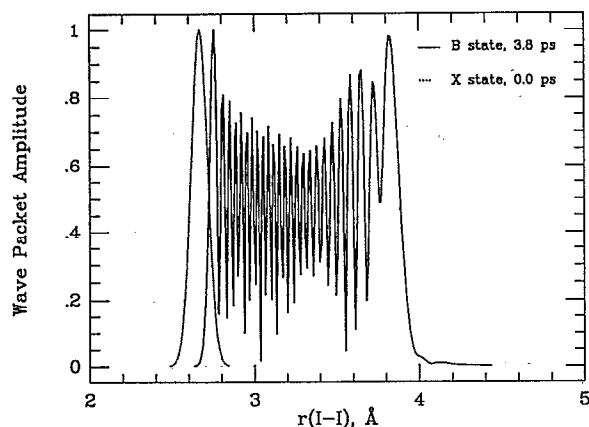
FIG. 18. Initial $v=0$ wave packet, and wave packet 3.8 ps after a 552 nm pump pulse in the B state of I_2. It has spread through the entire energetically accessible part of the potential well, and the node number indicates it is composed of vibrational eigenstates near $v=25$.

present experiments can be treated by second order perturbation theory of the pump–probe matter-radiation Hamiltonian; we chose laser pulse widths of 90 fs (FWHM Gaussian, taken in time to $\pm 2\sigma$), to match a temporal width. Wave packets were propagated using the Feit and Fleck split-operator technique.[27]

Figure 18 shows the original ground state wave function ($v=0$) and the B state wave packet 3.8 ps after termination of the pump pulse at 552 nm. As one might expect, the wave packet displays signs of nodal structure near $v=25$, which is the approximate vibrational quantum number of the eigenstates with the largest contribution to the wave packet. Figure 19 shows a longer time autocorrelation of the same wave packet, as well as its potential and kinetic energy expectation values. It can be seen that after about 10 ps, the packet behaves least like a single classical particle, being sufficiently delocalized to damp out fluctuations in the kinetic and potential energies.

Due to the large masses of the iodine atoms, the coherence behavior could be expected to be mimicked fairly closely by an ensemble of classically propagated particles with appropriate initial conditions. Figure 20 (top) shows the autocorrelation of the classical probability density functional $f[(x(t),p(t)]$ for 1000 particles. The initial position distribution used corresponds to the upper state wave packet density after the pump pulse from $v=0$ is over, and the *continuous* energy distribution is given by the laser profile. (We have chosen this initial distribution rather than a Wigner function because it is positive definite, and still fairly accurately reproduces the local energy vs position dependence of the initial wave packet in the B state.) This dephases after a few vibrational periods due to the lack of quantum coherence between *discrete* vibrational energy levels, and does not closely resemble the quantum autocorrelation function or the experimental transients. Figure 20 (bottom) shows a similar calculation, with the particles constrained to the *discrete* eigenvalues of our Morse model potential for the B state. This autocorrelation qualitatively resembles the quantum autocorrelation and
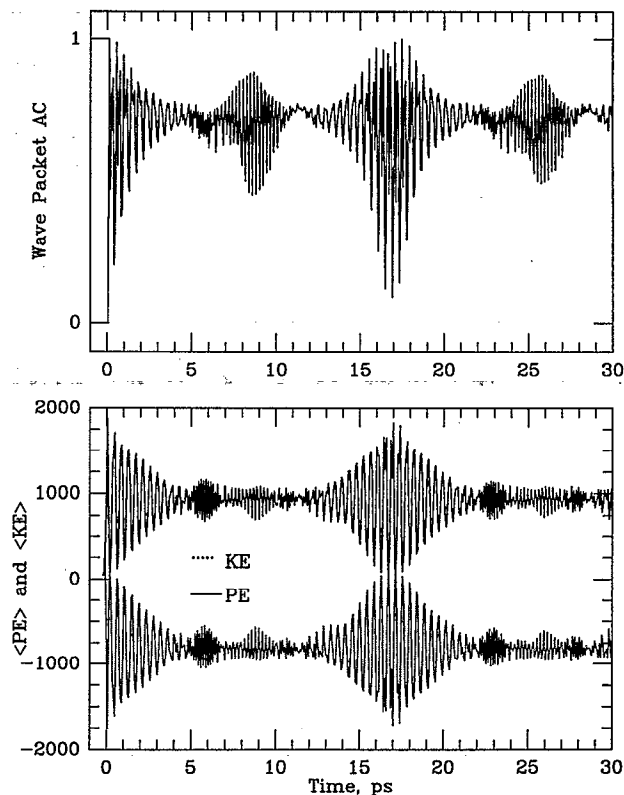

FIG. 19. Wave packet calculations on I_2; the upper figure shows an autocorrelation of the B state wave packet; the more "random" zones at 5, 11, and 22 ps correspond to a wave packet that has spread over the entire well and is quantal in nature; the lower figure shows the corresponding kinetic and potential energy expectation values.

experimental results, and shows rephasing due to the anharmonicity of the vibrational energy levels. Thus, at the very least a simple semiclassical model is required to model the experimentally observed transients.

We now return to the quantum calculations, and consider the effects of rotational and vibrational excitation on the calculated fluorescence signal from the f state. Figure 21 shows the effects on the vibrational transient of vibrational excitation in the absence of rotational excitation; the total fluorescence spectra pumped at 552 nm and probed at 310 nm are shown for initial vibrational levels of 0, 1, and 2. The fluorescence becomes increasingly structured with more nodes present in the initial wave function. The bottom of Fig. 21 shows a thermally (300 K) weighted average, which is considerably smoothed out. As expected, the second anharmonicity maximum near 17 ps (for the B state model surface) has the same amplitude as the $\tau=0$ maximum, since there is no rotational damping. At lower temperatures, the transient becomes increasingly like the $v=0$ one, showing more structure in the "dephased" region between maxima.

Figure 22 similarly shows the effects of rotational excitation on the transients. At the bottom is shown the result of a thermal average (with transients at J values other than 0,30,60,90 interpolated along both the amplitude *and*
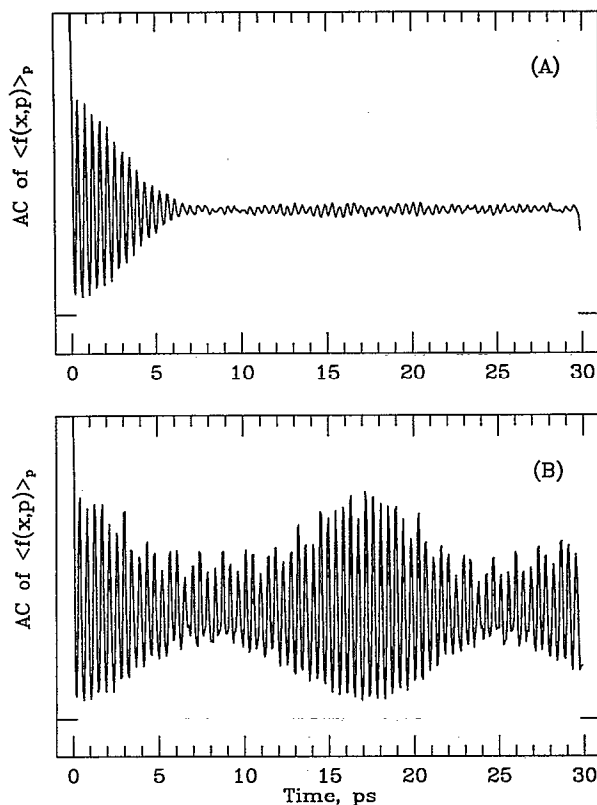
FIG. 20. Classical density functional autocorrelation functions for different initial conditions; the upper figure shows the autocorrelation for a set of particles spread over a continuous energy range within the laser bandwidth; the lack of coherence without a set of discrete energy levels is evident in the complete dephasing of the trace after several vibrational periods; the lower trace shows the autocorrelation for particles constrained to a discrete set of initial energies corresponding to the vibrational levels of the B state; as one might expect for a molecule as massive as I_2, this simple semiclassical approximation at least qualitatively reproduces the features of the quantum autocorrelation and experimental fluorescence transients.
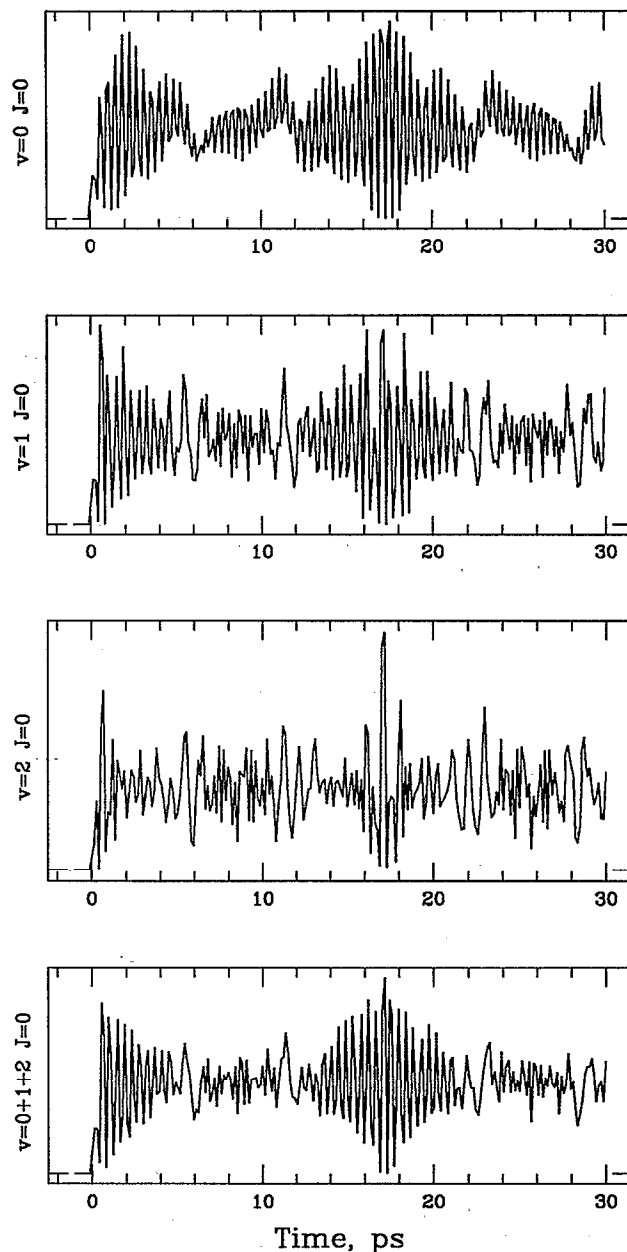

FIG. 21. Vibrational dependence of the detected fluorescence transient; the complexity of the structure is related to the complexity of the initial wave function; thermal averaging removes much of this structure (some slight irregularities are due to aliasing since the fluorescence spectrum was calculated at intervals of 67 fs).

time axes), with the damping effect, due to the slight continuous variation of the local vibrational frequency with J, clearly visible. The higher J transients also show a somewhat simpler behavior, with a "washed-out" region where the wave packet has dephased, as observed in the experimental room temperature transients.

Thus, the quantum simulations qualitatively bear out the smoothing of vibrational transients observed at higher temperatures, the effect of which is to allow simpler and more accurate fitting of the transients, rather than causing loss of information. While vibrational averaging alone can account for some smoothing, rotational averaging is required to explain the rapid damping of the "beat" maxima in the transient.

As a final point, we consider the effects of laser pulse shape and incoherence (nontransform limit) on the transients. We performed these calculations in the frequency domain, using the known FC factors (for the X–B transition) and energy levels. Figures 23(a) and 23(b) show a *full* simulation of the vibrational and rotational recurrences obtained with jitter-free, transform-limited Gauss-

ian pulses of FWHM 90 fs, using Eqs. (8) and (9). The main features of the magic angle transient resemble those of both the quantum-dynamics simulation and the 550 nm experiments, the differences being due to different assumptions about FC factors, the Morse approximation, or the different nature of the experimental laser pulses. The "noise" in the rotational transient 23b is remarkable in that it is also found experimentally, and is due to a highly dephased vibrational wave packet.

Figure 24(a) shows a similar calculation for non transform-limited pulses with a 90 fs FWHM Gaussian
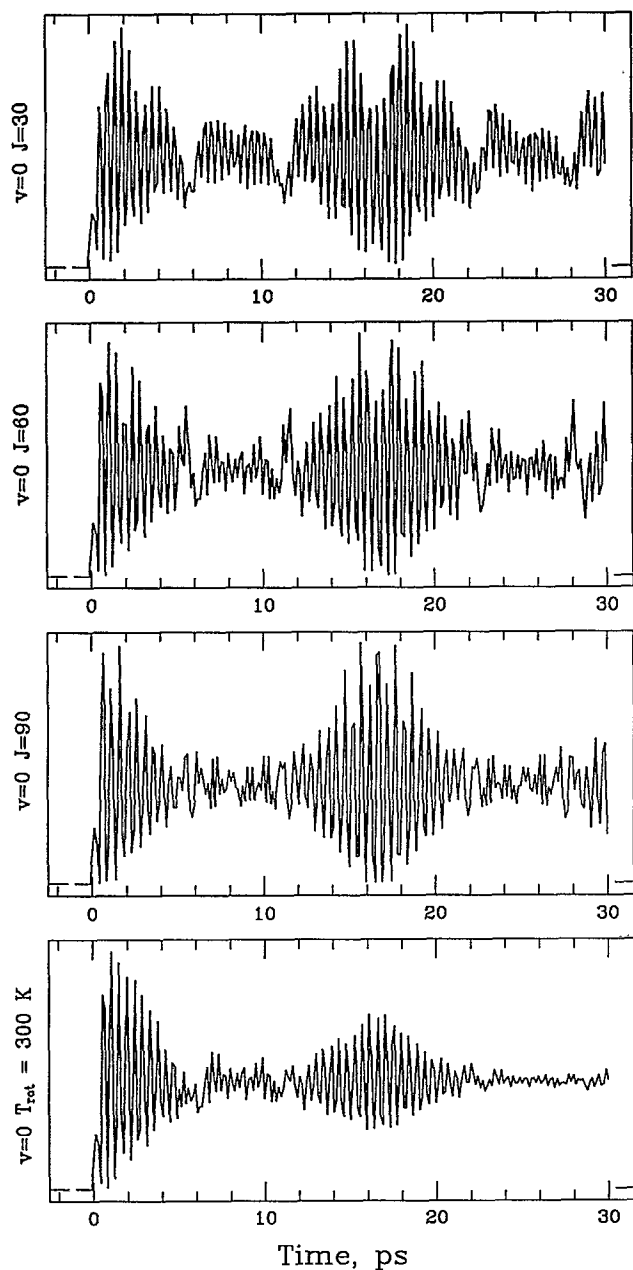
FIG. 22. Rotational dependence of the detected fluorescence transient; the rotational averaging is seen to lead to the damping described analytically by Eq. (14).
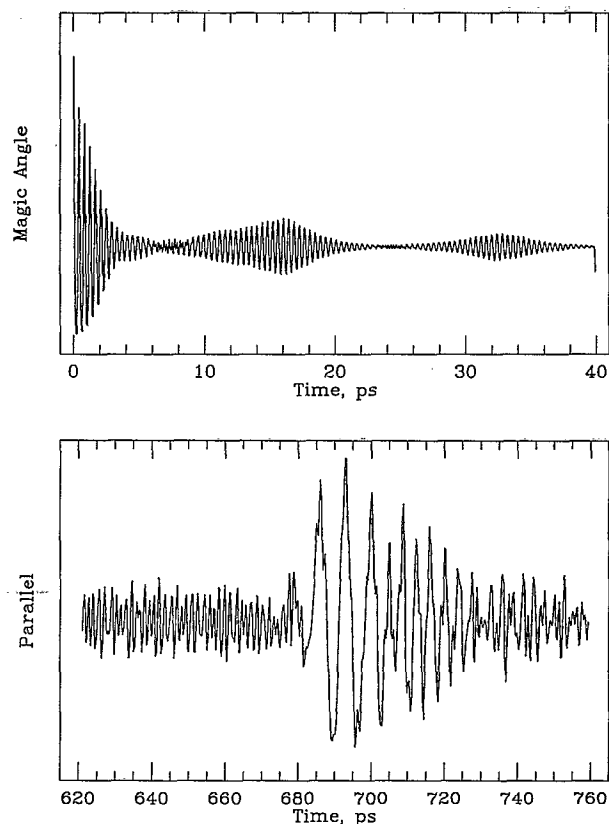

FIG. 23. Vibrational (magic angle) and rotational (parallel polarizations, full recurrence) transients calculated using Eqs. (8) and (9) for a Gaussian transform-limited beam of FWHM 90 fs.

extensively studied in nanosecond,[28] picosecond,[29] femtosecond experiments,[30] and in theory.[32]

VII. CONCLUSIONS

Femtosecond wave packet dynamics in isolated (collisionless) systems are discussed in relation to coherences (vibrational and rotational), vibration–rotation spectra and inversion to the potential. Experimental and theoretical results are presented for iodine, as an example, in gas-phase cells and in molecular beams. Other relevant systems are given in the work by the Gerber's group[33] and in Ref. 1. A number of interesting effects contribute to the appearance of FWS transients, and were considered here in attempts to quantify the dependence of the observed dynamics on coherences of nuclear vibrational and rotational motions.

Because FWS critically depends on coherent preparation of wave packets on a given potential, the method offers some unique features: (a) the separation of time scales for vibrational and rotational spectra (from measurements of *scalar* and *vector* properties of the dynamics), simplifying the analysis considerably; (b) the examination of *only* the potential on which coherence is formed (not the other two involved in the transitions), minimizing inhomogeneous broadening effects and providing information on spectrally congested, thermally heated samples; and (c) the ability to directly study the potential and spectra of bound *intermediates* in a chemical reaction. Some of the approaches pre-

temporal profile and a 10 nm square bandwidth profile (typical of continuum generation). Fig. 24b shows a transform-limited pulse with a 10 nm square bandwidth profile for comparison. These differences show how sensitive the transients are to the exact amplitudes A_{Vij} [and the partially randomized phase $\Delta\phi$ in Eq. (8)], even when the constituent frequencies are nearly identical. For example, the larger temporal width of the pulses in Fig. 24(a), compared to Fig. 24(b), leads to a clear reduction in higher frequency beats arising from more-than-once removed neighboring vibrational levels. The effects of pulse *shape*, *phase*, and *multiplicity* on coherent transients have been
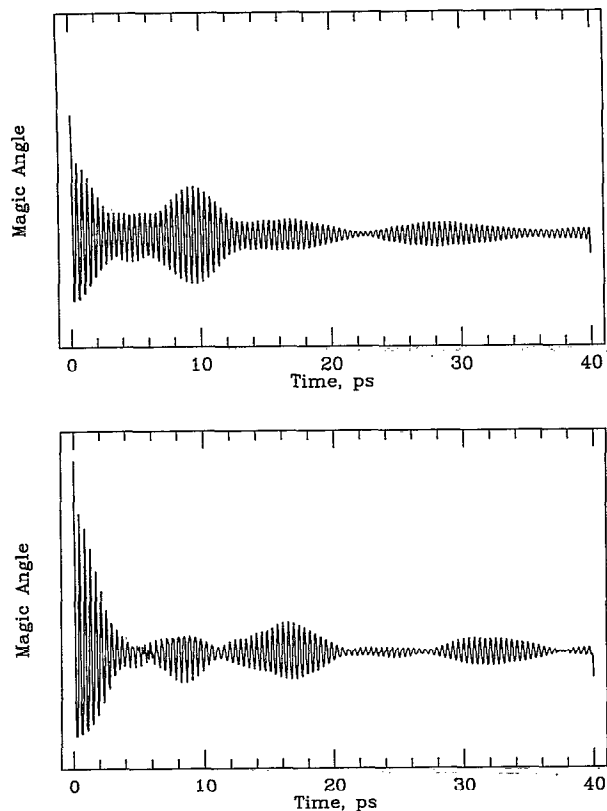
FIG. 24. Vibrational transients analogous to Fig. 23, but for laser pulses with gaussian temporal width of 90 fs and 10 nm square wavelength profile (upper) and same wavelength profile, but transform limited (lower).

sented here should prove useful in applications to complex systems where multiple potentials are involved or the dimensionality of the PES cannot be reduced to one.

ACKNOWLEDGMENT

[1] See: A. H. Zewail, Science **242**, 1645 (1988); L. R. Khundkar and A. H. Zewail, Ann. Rev. Phys. Chem. **41**, 15 (1990); A. H. Zewail, Faraday Discuss. Chem. Soc. **91**, 207 (1991), and references therein.

[2] See: P. M. Felker and A. H. Zewail, Adv. Chem. Phys. **70**, 265 (1988); M. Cote, J. F. Kaufmann, P. G. Smith, and J. D. McDonald, J. Chem. Phys. **90**, 2865 (1989); W. R. Lambert, P. M. Felker and A. H. Zewail, *ibid.* **75**, 5958 (1981); A. J. Kaziska and M. R. Topp, Chem. Phys. Lett. **180**, 423 (1991); M. Ivanco, J. Hager, W. Sharfin, and S. C. Wallace, J. Chem. Phys. **78**, 6531 (1983); J. M. Smith, C. Lakshminarayan, and J. L. Knee, *ibid.* **93**, 4475 (1990); P. M. Felker, J. Phys. Chem. **96**, 7844 (1992), and references therein.

[3] M. Dantus, R. M. Bowman, and A. H. Zewail, Nature (London) **343**, 737 (1990).

[4] H. Bitto and J. R. Huber, Acc. Chem. Res. **25**, 65 (1992), and references therein.

[5] M. Gruebele, G. Roberts, M. Dantus, R. M. Bowman, and A. H. Zewail, Chem. Phys. Lett. **166**, 459 (1990).

[6] M. H. M. Janssen, R. M. Bowman, and A. H. Zewail, Chem. Phys. Lett. **172**, 99 (1990); R. B. Bernstein and A. H. Zewail, *ibid.* **170**, 321 (1990).

[7] S. Gerstenkorn and P. Luc, J. Phys. (Paris) **46**, 867 (1985); R. S. Mulliken, J. Chem. Phys. **55**, 288 (1971).

[8] R. M. Bowman, M. Dantus and A. H. Zewail, Chem. Phys. Lett. **161**, 297 (1989).

[9] See J. C. D. Brand and A. R. Hoy, Can. J. Phys. **60**, 1209 (1982); R. J. Donovan, A. J. Holmes, P. R. R. Langridge-Smith, and T. Ridley, J. Chem. Soc. Faraday Trans. **85**, 541 (1988).

[10] P. M. Felker and A. H. Zewail, J. Chem. Phys. **86**, 2460 (1987); Adv. Chem. Phys. **70**, 265 (1988).

[11] R. M. Bowman, M. Dantus, and A. H. Zewail, Chem. Phys. Lett. **174**, 546 (1990).

[12] M. Dantus, M. H. M. Janssen, and A. H. Zewail, Chem. Phys. Lett. **181**, 281 (1991).

[13] E. D. Potter, J. Herek, Q.-L. Liu, S. Pedersen, and A. H. Zewail, Nature (London) **355**, 66 (1992).

[14] A. B. Myers and R. M. Hochstrasser, J. Chem. Phys. **85**, 6301 (1986), and references therein.

[15] G. V. Hartland, L. L. Connell, and P. M. Felker, J. Chem. Phys. **94**, 7649 (1991); G. V. Hartland, P. W. Joireman, L. L. Connell, and P. M. Felker, *ibid.* **96**, 179 (1992).

[16] S. Mukamel, Ann. Rev. Phys. Chem. **41**, 647 (1990); *Density Matrix Methods and Femtosecond Processes*, edited by S. H. Lin (World Scientific, Singapore, 1991); W. T. Pollard, H. L. Fragnito, J. Y. Bigot, C. V. Shank, and R. A. Mathies, Chem. Phys. Lett. **168**, 239 (1990).

[17] S. M. Kay and S. L. Marple, Jr., Proc. IEEE **69**, 1380 (1981).

[18] C. Schwartz and R. J. Leroy, J. Chem. Phys. **81**, 3996 (1984), and references therein.

[19] M. Gruebele, Mol. Phys. **69**, 475 (1990).

[20] R. J. Le Roy and R. B. Bernstein, J. Mol. Spectrosc. **37**, 109 (1971).

[21] H. Metiu and V. Engel, J. Chem. Phys. **93**, 3252 (1990).

[22] R. Kosloff and A. Dell Hammerich, Faraday Discuss. Chem. Soc. **91**, 239 (1991), and references therein.

[23] S. O. Williams and D. G. Imre, J. Chem. Phys. **92**, 6636, 6648 (1988).

[24] V. Engel, H. Metiu, R. Almeida, R. A. Marcus, and A. H. Zewail, Chem. Phys. Lett. **152**, 1 (1988); V. Engel and H. Metiu, J. Chem. Phys. **90**, 6116 (1989); Ch. Meier, V. Engel and J. S. Briggs, *ibid.* **95**, 7337 (1991).

[25] B. Hartke, J. Manz, and J. Mathis, Chem. Phys. **139**, 123 (1989); B. Hartke, Chem. Phys. Lett. **175**, 322 (1990).

[26] M. Gruebele, G. Roberts, and A. H. Zewail, Philos. Trans. R. Soc. London, Ser. A **332**, 223 (1990); G. Roberts and A. H. Zewail, J. Phys. Chem. **95**, 7973 (1991).

[27] M. D. Feit, J. A. Fleck, Jr., and A. Steiger, J. Comput. Phys. **47**, 412 (1982).

[28] W. S. Warren and A. H. Zewail, J. Chem. Phys. **75**, 5956 (1981); **78**, 2279 (1983).

[29] J. P. Heritage, T. K. Gustavson, and C. H. Lin, Phys. Rev. Lett. **34**, 1299 (1975); W. S. Warren, Science **242**, 876 (1988).

[30] N. F. Scherer, A. J. Ruggiero, M. Du, and G. R. Fleming, J. Chem. Phys. **93**, 856 (1990); N. F. Scherer, R. J. Carlson, A. Matro, M. Du, A. J. Ruggiero, V. Romerorochin, J. A. Cina, G. R. Fleming, and S. A. Rice, *ibid.* **95**, 1487 (1991); A. M. Weiner, J. P. Heritage and E. M. Kirschner, J. Opt. Soc. Am. **85**, 1563 (1988); A. M. Weiner, D. E. Leaird, G. P. Wiederrecht, and K. A. Nelson, Science **247**, 1317 (1990); J. Gerdy, M. Dantus, R. Bowman, and A. H. Zewail, Chem. Phys. Lett. **171**, 1 (1990).

[31] R. F. Barrow and K. K. Yee, J. Chem. Soc. Faraday Trans. 2 **69**, 684 (1973).

[32] For a review, see D. J. Tannor and S. A. Rice, Adv. Chem. Phys. LXX (Part 1), 441 (1988); Also, J. Cina, Phys. Rev. Lett. **66**, 1146 (1991); E. Kolba and J. Manz, Faraday Discuss. Chem. Soc. **91**, 369 (1991), and papers in this Discussion volume. For work on the theoretical consideration of multiple pulse and phase-coherent pulses, see also Ref. 28.

[33] T. Banmert, V. Engel, C. Röttgermann, W. T. Strunz, and G. Gerber, Chem. Phys. Lett. **191**, 639 (1992); J. Phys. Chem. **95**, 8103 (1991); T. Banmert, M. Grosser, R. Thalweiser, and G. Gerber, Phys. Rev. Lett. **67**, 3753 (1992).